

Optical and Near-infrared Observations of SN 2023ixf for over 600 days after the Explosion

Gaici Li¹, Xiaofeng Wang^{1*}, Yi Yang^{1,2}, A. Pastorello³, A. Reguitti^{4,3}, G. Valerin³, P. Ochner^{5,3}, Yongzhi Cai^{6,7,8}, T. Iijima³, U. Munari³, I. Salmaso^{9,3}, A. Farina⁵, R. Cazzola⁵, N. Trabacchin¹⁰, S. Fiscale^{11,12}, S. Ciroi^{5,3}, A. Mura^{5,3}, A. Siviero^{5,3}, F. Cabras⁵, M. Pabst⁵, S. Taubenberger¹³, C. Vogl¹³, C. Fiorin, Jialian Liu¹, Liyang Chen¹, Danfeng Xiang^{14,1}, Jun Mo¹, Liping Li^{6,7,8}, Zhenyu Wang^{6,7,8,15}, Jujia Zhang^{6,7,8}, Qian Zhai^{6,8}, D.O. Mirzaqulov¹⁶, S.A. Ehgamberdiev^{16,17}, Alexei V. Filippenko², Shengyu Yan¹, Maokai Hu¹, Xiaoran Ma¹, Qiqi Xia^{1,18}, Xing Gao¹⁹, and Wenxiong Li²⁰

(Affiliations can be found after the references)

April 8, 2025

ABSTRACT

Context. We present a comprehensive photometric and spectroscopic study of the nearby Type II supernova (SN) 2023ixf, with our extensive observations spanning the phases from ~ 3 to over 600 days after the first light.

Aims. The aim of this study is to obtain key information on the explosion properties of SN 2023ixf and the nature of its progenitor.

Methods. The observational properties of SN 2023ixf are compared with those of a representative sample of Type IIP/IIL SNe to investigate commonalities and diversities. We conduct a detailed analysis of temporal evolution of major spectral features observed throughout different phases of the SN 2023ixf explosion. Several key interpretations are addressed through a comparison between the data and the model spectra predicted by non-local thermodynamic equilibrium (non-LTE) radiative-transfer calculations for progenitor stars within a range of zero-age main sequence (ZAMS) masses.

Results. Our observations indicate that SN 2023ixf is a transitional SN that bridges the gap between Type IIP and IIL subclasses of H-rich SNe, characterized by a relatively short plateau ($\lesssim 70$ d) in the light curve. It shows a rather prompt spectroscopic evolution toward the nebular phase; emission lines of Na, O, H, and Ca in nebular spectra all exhibit multipeak profiles, which might be attributed to bipolar distribution of the ejecta. In particular, the H α profile can be separated into two central peaked components (with a velocity of about 1500 km s^{-1}) that is likely due to nickel-powered ejecta and two outer peak/box components (with a velocity extending up to $\sim 8000 \text{ km s}^{-1}$) that can arise from interaction of the outermost ejecta with a circumstellar shell at a distance of $\sim 6.2 \times 10^{15} \text{ cm}$. The nebular-phase spectra of SN 2023ixf show good agreement with those predicted by a non-LTE radiative-transfer code for progenitor stars with a ZAMS mass ranging from 15 to $19 M_{\odot}$. A distance $D = 6.35^{+0.31}_{-0.39} \text{ Mpc}$ is estimated for M101 based on the expanding photosphere method.

Key words. stars: massive – stars: mass-loss – supernovae: individual: SN 2023ixf

1. Introduction

Core-collapse supernovae (CCSNe) are terminal explosions of massive stars with zero-age main sequence (ZAMS) masses larger than $\sim 8 M_{\odot}$. Observational properties among H-rich (or Type II) CCSNe span a broad parameter space, suggesting intrinsic diversity in progenitor properties and explosion mechanisms (Smartt et al. 2009; Smartt 2009; Li et al. 2011; Smartt 2015). Two subclasses have been established solely based on the light-curve morphology, namely Type II-linear (SN IIL) and Type II-plateau (SN IIP; Barbon et al. 1979). The former shows a post-peak linear magnitude decline at a pace of $\sim 0.5 \text{ mag } 100 \text{ d}^{-1}$, lasting $\lesssim 80$ – 100 days (e.g., Li et al. 2011; Anderson et al. 2014), while the latter maintains a rather constant brightness for ~ 100 – 140 days after the light-curve peak (Anderson et al. 2014). Such a light-curve plateau can be understood as a consequence of the emission released by re-

combination of hydrogen in the outermost envelope of the SN ejecta (Popov 1993; Zampieri et al. 2003; Nakar & Sari 2010). These modeling efforts suggest that the difference in the light-curve morphology of the SN IIP and SN IIL subclasses can be attributed to the remaining mass and radial density profile of the H-rich envelope of their massive progenitors.

It also remains debated whether the light-curve decline rates of SNe IIP and IIL follow a distinct (Arcavi et al. 2012; Faran et al. 2014) or continuous (Anderson et al. 2014; Sanders et al. 2015) distribution. In some cases, spectra of SNe II present a series of strong hydrogen Balmer lines with a low velocity (~ 20 – 800 km s^{-1} ; see Smith 2017; Yang et al. 2023, and references therein), which can remain visible even years after the explosion. These objects have been classified as Type II-narrow (II_n) SNe (Schlegel 1990), for which the narrow Balmer lines arise from the ionized circumstellar matter (CSM) previously expelled from the progenitor star. Such an enrichment procedure of

* E-mail: wang_xf@mail.tsinghua.edu.cn

the CSM may exhibit a continuous wind-like process or multiple episodes of mass ejections prior to the terminal explosion.

Recent observations of SNe II starting $\lesssim 1$ day after the explosion have identified elevated mass loss immediately before the explosion. As a result, the ambient CSM will manifest as shock-breakout flash-ionized spectral features (Quimby et al. 2007; Gal-Yam et al. 2014; Yaron et al. 2017; Zimmerman et al. 2024), which have been found in more than half of their massive progenitors (Bruch et al. 2021, 2023). As the ionization states of various atoms in the CSM are highly dependent on the injected energy, and they can be quickly swept away by the rapidly expanding ejecta owing to their vicinity, these “flash” features may persist for only a few days. Therefore, the line species identified in the prompt, flash-ionized spectral features closely trace the surface chemical composition of the exploding progenitor. The temporal evolution of the line strength also results from an interplay between the pre-explosion mass-loss history and the radial profile of the ionization states in the CSM. Despite its ubiquity, however, the mechanism driving such enhanced mass loss within years of the terminal explosion remains unclear. When the ejecta engulf the CSM, the outermost layer is dominated by the expanding H envelope, displaying broad P Cygni profiles of Balmer lines.

Apart from the enigmatic enhanced pre-explosion mass loss, efforts have also been made to investigate the core-collapse process. Recent three-dimensional (3D) numerical calculations have been successful in exploding massive stars. After the initial core collapse, the outward transport of energy produced by the initial bounce shock is facilitated by absorbing neutrinos (Burrows & Vartanyan 2021; Burrows et al. 2024; Wang & Burrows 2024; Vartanyan et al. 2024). Alternative models may involve energy deposition in the stellar envelope and the launch of moderately relativistic jets (LeBlanc & Wilson 1970; Khokhlov et al. 1999; Maeda & Nomoto 2003; Obergaulinger et al. 2014; Mösta et al. 2015; Janka et al. 2016; Soker 2016).

While spectrophotometric monitoring starting from the earliest phases provides critical characteristics of the energy, chemical content, and kinematics of the SN explosion, observations at later phases yield highly complementary information that is essential to probe the explosion physics. After most of the H envelope has recombined, the late-time emission is powered by the radioactive decay of iron-group elements such as Ni and Co. These heavy nuclei were synthesized by the shock near the explosion center. As the nucleosynthesis depends strongly on the ZAMS mass of the star (e.g., Woosley et al. 1995), the spectral features of the newly synthesized elements (e.g., C, O, Si, Ca, Fe, Co, and Ni) provide unique fingerprints of the explosion physics at work. Therefore, the line species, the ionization states, and the line profiles may provide critical clues about (respectively) the explosion core’s chemical composition, physical conditions, and dynamics, thereby linking the progenitor properties and the explosion mechanism (e.g., Jerkstrand 2017). The deep interior is revealed only as the optical depth of the ejecta progressively decreases with time.

SN2023ixf was discovered as a young SN candidate in the nearby spiral galaxy Messier 101 (M101, also known as NGC 5457) on 2023-05-19 17:27:15 (UTC dates are used

throughout this paper) / MJD 60083.72726 by Koichi Itagaki (Itagaki 2023). In this paper, we adopt a distance to M101 of 6.85 ± 0.15 Mpc (Riess et al. 2022). The first classification spectrum obtained at 2023 05-19 22:23 / MJD 60083.93 shows a set of narrow emission lines of H, He, C, and N superimposed on a blue continuum (Perley & Gal-Yam 2023). The profiles of these emission lines have full-widths at half-maximum (FWHMs) of $\lesssim 1000\text{--}2000$ km s $^{-1}$ and centered at zero velocity relative to the redshift $z = 0.000804$ of its host (Riess et al. 2022). The observational signatures suggested a young, Type II nature for SN2023ixf (Perley & Gal-Yam 2023). The narrow features persisted for the first few days, with the most prominent H α line being still visible ~ 10 days after the explosion. Such signatures in the early spectroscopic time sequence of SN2023ixf suggest that the progenitor experienced an enhanced mass loss prior to the explosion, building up dense CSM that extends up to $\sim 10^{14}$ cm (Bostroem et al. 2023; Hiramatsu et al. 2023; Smith et al. 2023; Teja et al. 2023; Zhang et al. 2023; Zheng et al. 2025).

The progenitor of SN2023ixf has been identified in archival images obtained by the *Hubble Space Telescope* (HST) and the *Spitzer Space Telescope* (Spitzer). Comparisons between the fitting to the spectral energy distribution (SED) of the pre-explosion source and stellar evolutionary tracks indicate a red supergiant (RSG) progenitor enshrouded by a dusty shell. However, a broad mass range of the progenitor has been found, ~ 8 to $20 M_{\odot}$ (Pledger & Shara 2023; Kilpatrick et al. 2023; Xiang et al. 2024; Van Dyk et al. 2024a; Jencson et al. 2023; Niu et al. 2023; Qin et al. 2024; Soraisam et al. 2023).

Several unprecedented datasets also provide key diagnostics of the explosion geometry. For example, a series of high-resolution spectra within the first week of the explosion revealed discrepancies among the evolution of the spectral profiles measured from different ionization states, which can be attributed to asymmetry in the dense CSM (Smith et al. 2023). The dramatically changing spectropolarimetric properties of SN2023ixf measured between ~ 1.4 and 14.5 days after the explosion depict aspherical, optically thick CSM swept away by the aspherical SN ejecta within the first ~ 5 days (Vasylyev et al. 2023). The initial reddish color that evolved blueward measured from as early as ~ 1.4 hr after the explosion is indicative of the gradual sublimation of pre-SN dust grains as the shock-breakout front propagates through an aspherical shell of CSM (Li et al. 2024).

The comparisons of the nebular spectra of SN2023ixf with model spectra suggest that its progenitor mass ranges from 10 to $16 M_{\odot}$ (Michel et al. 2025; Kumar et al. 2025; Folatelli et al. 2025; Zheng et al. 2025; Fang et al. 2024; Ferrari et al. 2024). A boxy-shaped emission of H α is observed during the nebular phase, which hints at interaction between the ejecta and a CSM shell (Michel et al. 2025; Kumar et al. 2025; Folatelli et al. 2025; Zheng et al. 2025; Ferrari et al. 2024).

This paper presents extensive optical photometry and optical/near-infrared (NIR) spectroscopy of SN2023ixf spanning from the first day to over 600 days after the explosion. Our observations and data reduction are outlined in Section 2. In Section 3 we discuss the photometric evolution. Section 4 details the spectral evolution. Implications of the observational proper-

ties are discussed in Section 5, and our concluding remarks are provided in Section 6.

2. Observations

2.1. Photometry

Optical photometry of SN 2023ixf was obtained with the 0.8 m Tsinghua University-NAOC telescope (hereafter TNT; Huang et al. 2012) at Xinglong Observatory in China, the 1.5 m AZT-22 telescope (hereafter AZT; Ehgamberdiev 2018) at the Maidanak Astronomical Observatory (MAO) in Uzbekistan, the Lijiang 2.4 m telescope (hereafter LJT; Fan et al. 2015) of Yunnan Astronomical Observatories in China, and the Schmidt 67/91 cm Telescope (hereafter 67/91-ST) and 1.82 m Copernico Telescope (hereafter Copernico) at the Asiago Astrophysical Observatory in Italy. NIR photometry in the *JHK* bandpasses was obtained with the Near Infrared Camera Spectrometer (NICS; Baffa et al. 2001) mounted on the 3.58 m Telescopio Nazionale Galileo (TNG; Barbieri et al. 1994) on the island of La Palma. The photometry is provided in Table 1. All phases are given relative to the time of the first light estimated by Li et al. (2024) (MJD 60082.788) throughout the paper.

Table 1. Observed photometry of SN 2023ixf

MJD	Phase (d)	Filter	Mag	err	Instrument
60086.612	3.824	U	10.064	0.064	XLT
60086.612	3.824	B	11.128	0.051	XLT
60086.612	3.824	V	11.376	0.048	XLT
60086.624	3.836	g	10.812	0.083	XLT
60086.624	3.836	r	11.413	0.046	XLT
60086.624	3.836	i	11.611	0.029	XLT
60087.000	4.212	u	10.926	0.113	67/91 ST
60087.000	4.212	g	10.963	0.038	67/91 ST
...

Note : This table is available in its entirety in machine-readable form.

Optical images obtained by all facilities were reduced following standard procedures, including bias subtraction and flat-field correction. Images obtained by the TNT were processed using a custom “ZURTYPHOT” pipeline (Mo et al., in prep.). Reduction of the AZT, LJT, Copernico, and 67/91-ST images was carried out using the AUTOPHOT pipeline (Brennan & Fraser 2022). The World Coordinate System (WCS) was solved using ASTROMETRY.NET (Lang et al. 2010). We performed point-spread-function (PSF) photometry on the images; however, for accurate results, template subtraction might be required for photometry obtained at day 625 after the explosion.

For all *BVgri*-band images, photometry is also performed to extract the instrumental magnitudes of any bright field stars that have photometric data available from the AAVSO Photometric All Sky Survey (APASS) DR9 Catalogue (Henden et al. 2016). By employing magnitudes of these local bright and isolated comparison stars, instrumental *BV*- and *gri*-band magnitudes of SN 2023ixf were calibrated to the standard Johnson *BV*

system (Johnson et al. 1966) in Vega magnitudes and the Sloan Digital Sky Survey (SDSS) photometric system (Fukugita et al. 1996) in AB magnitudes, respectively. The instrumental *uz*-band magnitudes were calibrated using SDSS Release 16 (Ahumada et al. 2020) to the standard SDSS photometric system. Instrumental *U*-band magnitudes of SN 2023ixf were converted to Johnson *U* using the standard stars of Zhang et al. (2016b). After the calibration of the instrumental magnitudes, we found that the *V*-band magnitudes from AZT show a systematic difference from those of other facilities by ~ 0.15 mag, likely caused by the deviation of the throughput from the standard system. Therefore, color-corrections have been applied to the *V*, *B*, and *U* photometry (Landolt 1992) from the AZT images.

The NIR images were processed including flat-field and bias correction. Standard IRAF¹ (Tody 1986, 1993) tasks were used to reduce the TNG/NICS images. Instrumental magnitudes were measured using SNOOPY², and calibrated using the Two Micron All Sky Survey (2MASS³, Skrutskie et al. (2006)) catalog.

2.2. Spectroscopy

The spectroscopic campaign for SN 2023ixf spans days +3 to +324. Optical observations were carried out using the following facilities.

- (i) The Asiago Faint Object Spectrograph and Camera (AFOSC) on the 1.82 m Copernico telescope operated by INAF Astronomical Observatory of Padova, atop Mount Ekar (Asiago, Italy).
- (ii) The 1.22 m Galileo Telescope (hereafter GT) equipped with the B&C spectrograph at Osservatorio Astronomico di Asiago, Asiago, Italy.
- (iii) the Beijing Faint Object Spectrograph and Camera (BFOSC) mounted on the Xinglong 2.16 m telescope (hereafter XLT; Zhang et al. 2016a), China.
- (iv) The 2.4 m LJT equipped with YFOSC (Yunnan Faint Object Spectrograph and Camera. Wang et al. 2019).

Seven NIR spectra were taken by the NICS instrument on the TNG, spanning the phase interval from days 4 to 93. Logs of the optical and NIR spectroscopy are presented in Tables A.1 and A.2, respectively.

All spectra except for those from XLT were obtained with the long slit aligned at the parallactic angle (Filippenko 1982). Spectra obtained with Copernico/AFOSC were reduced using the dedicated pipeline FosCGUI.⁴ Spectroscopic data obtained by other facilities were reduced utilizing standard IRAF routines including bias subtraction, flat-field correction, and re-

¹ IRAF is distributed by the National Optical Astronomy Observatories, which are operated by the Association of Universities for Research in Astronomy, Inc., under cooperative agreement with the U.S. National Science Foundation.

² SNOOPY is a package for SN photometry using PSF fitting and/or template subtraction developed by E. Cappellaro. A package description can be found at <https://sngroup.oapd.inaf.it/snoopy.html>

³ <http://irsa.ipac.caltech.edu/Missions/2mass.html/>

⁴ FosCGUI is a graphical user interface (GUI) dedicated to extract the photometry and spectroscopy obtained with FOSC-like instruments. It was developed by E. Cappellaro. A package description can be found at <https://sngroup.oapd.inaf.it/foscgui.html>

removal of cosmic rays. Wavelength calibration was carried out using comparison-lamp exposures. Flux calibration was performed using the sensitivity functions derived from the spectra of photometric standard stars observed during the same night, at airmasses similar to that of SN 2023ixf. Atmospheric extinction was corrected using the extinction curves of the observatories, and telluric lines were removed using the standard-star spectra.

3. Photometric Evolution

We estimate the Galactic reddening component along the SN 2023ixf line of sight as $E(B - V)_{23ixf}^{MW} = 0.008$ mag by querying the NASA/IPAC NED⁵ Galactic Extinction Calculator, based on the extinction map derived from Schlafly & Finkbeiner (2011). Reddening due to the host galaxy was estimated as $E(B - V)_{23ixf}^{host} = 0.032$ mag according to the equivalent width of the Na I D absorption lines measured from the high-resolution spectra of SN 2023ixf (Smith et al. 2023; Teja et al. 2023; Zhang et al. 2023) and the empirical relation derived between the line width and the dust reddening (Poznanski et al. 2012). Thus, the total reddening is estimated as $E(B - V)_{23ixf}^{total} = 0.04$ mag.

After correcting for the Galactic and host-galaxy extinction, the *UuBgVrizJHK*-band light curves of SN 2023ixf are presented in Fig. 1, covering phases from 3 to 625 days after the explosion. A more thorough investigation of the photometric properties within the first hours to a few days is presented by Li et al. (2024). The *V* light curve of SN 2023ixf indicates a rise of ~ 6 days before a peak magnitude of $M_V^{peak} = -18.0 \pm 0.1$ is reached. The high peak luminosity places SN 2023ixf near the bright end of SNe II as illustrated by detailed sample analyses (e.g., de Jaeger et al. 2019).

Following Anderson et al. (2014) and using the *V* light curve of SN 2023ixf, we derive the s_1 and s_2 parameters as 3.35 ± 0.13 and 1.93 ± 0.10 mag per 100 days, respectively. The former and the latter describe the magnitude decline rate measured from the time between the peak luminosity and the start of the linearly declining plateau, and the magnitude decline rate when the SN has settled on its plateau phase, respectively. These derived results are consistent with those measured by (Zheng et al. 2025). These values indicate an overall steeper decline compared to the corresponding mean values measured from the sample of Anderson et al. (2014), which are 2.65 mag and 1.47 mag per 100 days, respectively.

After ~ 70 days, the *V* light curve of SN 2023ixf shows a transition from the plateau phase to the radioactive tail. During the phase between 100 and 300 days after the explosion, the *V*-band decline rate is measured to be 1.23 ± 0.01 mag $(100 \text{ d})^{-1}$. Such a rate appears to be faster compared to that expected for the $^{56}\text{Co} \rightarrow ^{56}\text{Fe}$ decay, ~ 0.98 mag $(100 \text{ d})^{-1}$, as shown in Fig. 1. This indicates that γ -ray photons are not fully trapped inside the ejecta at this late phase.

In Fig. 2, we compare the absolute *V* light curve of SN 2023ixf with those of a selected sample of well-studied Type II SNe, including Type IIP SNe 1999em (Leonard et al. 2002) and 2017gmr (Andrews et al. 2019), Type IIP/L SN 2013ej (Huang et al. 2015), Type II short-plateau SN

2006ai (Hiramatsu et al. 2021), and Type IIL SNe 1980K (Buta 1982) and 1990K (Cappellaro et al. 1995). All light curves have been corrected for extinction in both the host galaxy and the Milky Way.

The *V* light curve of SN 2023ixf shows a brighter absolute peak magnitude and shorter plateau compared to that of the prototypical SN IIP SN 1999em. A shorter and less prominent plateau can also be identified in the light curves of SN 2006ai and Type IIP/IIL SN 2013ej (Bose et al. 2015). The short-plateau Type II SN 2006ai, as discussed by Hiramatsu et al. (2021), is indicative of having a less massive H-rich envelope in its progenitor compared to that of normal SNe IIP (Hillier & Dessart 2019). The *V* light curves of Type IIL SNe 1980K and 1990K exhibit a much faster and more linear post-peak decline than that of SN 2023ixf during the plateau phase. Based on the comparison results discussed above, we suggest that SN 2023ixf may be best described as a transitional object between Type IIP and IIL in terms of post-peak photometric evolution.

4. Spectroscopic Evolution

4.1. Optical Spectroscopy

In Fig. A.1, we present the spectral time series of SN 2023ixf observed by XLT, Copernico, GT, NOT, and LJT from days 3 to 324. All spectra are corrected for the redshift $z = 0.000804$ of its host galaxy (Riess et al. 2022) and dereddened adopting a total line-of-sight extinction $E(B - V)_{23ixf}^{total} = 0.04$ mag.

Narrow emission lines including H, He II, and C IV remain prominent within the first three days after the explosion. The “flash features” at high excitation states arise from the shock-ionized species in the CSM shell in close vicinity of the exploding progenitor. This material was most likely expelled by pre-explosion instabilities in the years leading to the terminal SN explosion, and the spectral signatures reflect the surface composition of the dying progenitor and trace the explosion and shock physics of the SN. Comprehensive analyses of the intranight spectroscopic evolution of SN 2023ixf starting from day 1 has been carried out by Bostroem et al. (2023), Zheng et al. (2025), Hiramatsu et al. (2023), Smith et al. (2023), Teja et al. (2023), and Zhang et al. (2023). As illustrated in Fig. A.1, the flash features superimposed on the blue continuum persist for the first eight days.

Broad P Cygni profiles emerged for spectral lines of Ba II, Fe II, Sc II and Na I after the flash features were gone. A prominent H α P Cygni line is seen after approximately day 20, indicating that the emission is dominated by the expanding H-rich envelope of the ejecta. Absorption on the blue side of H α at $\sim 13,000 \text{ km s}^{-1}$ appears at ~ 20 d and disappears at ~ 90 d. This notch was previously attributed to the high-velocity component of H α (Leonard et al. 2002; Baron et al. 2000) or Si II $\lambda 6355$ (Pastorello et al. 2006; Valenti et al. 2014). The blue continuum diminishes as the SN enters the nebular phase.

At about 90 days after explosion, the photosphere recedes through the H envelope. The absorption component of the P Cygni profile of H α disappears and forbidden metal emission

⁵ <https://ned.ipac.caltech.edu/>

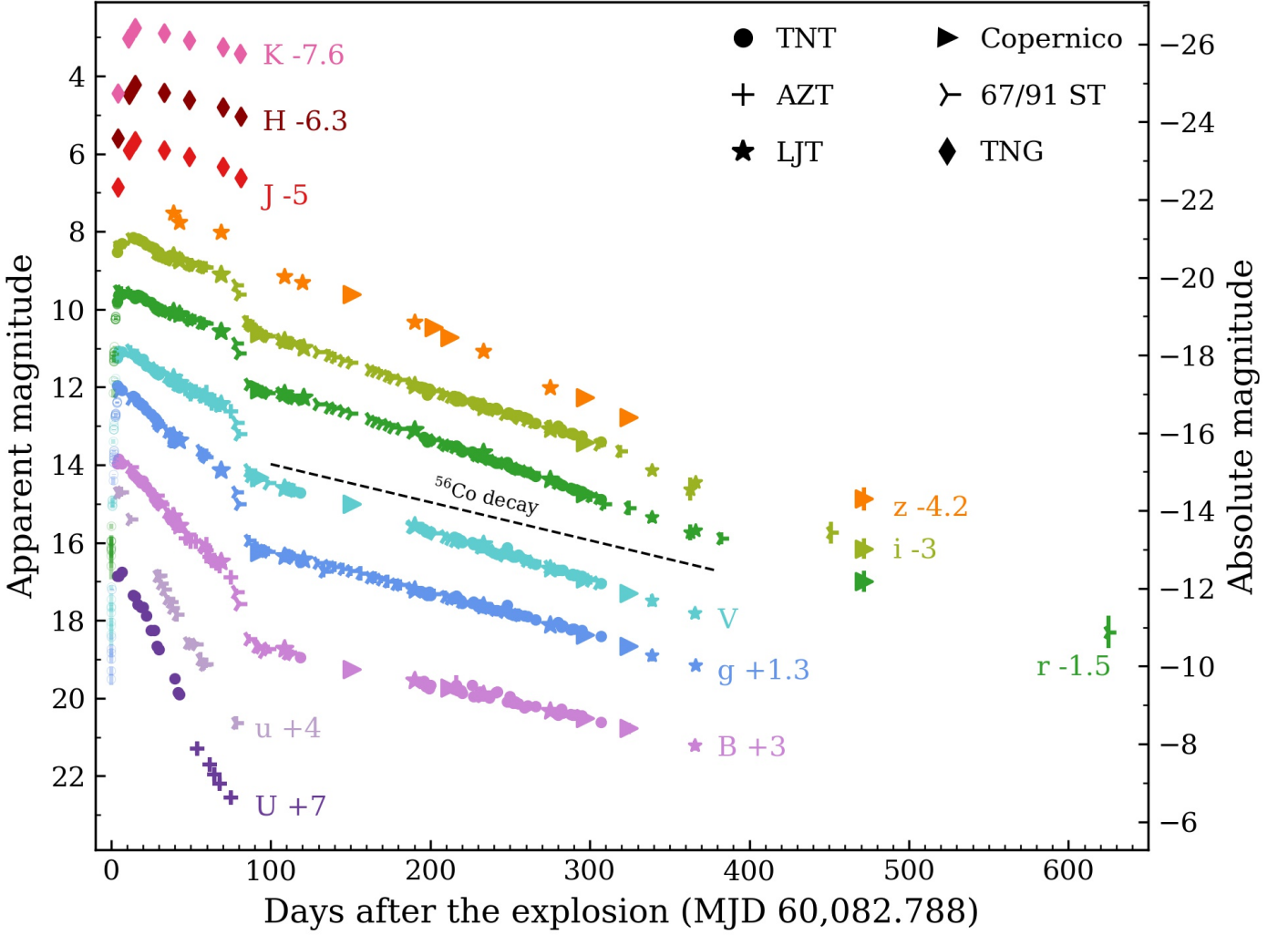


Fig. 1. Optical and NIR light curves of SN 2023ixf. Open circles overplot the early g -, V -, and r -band light curves from Li et al. (2024). The black dashed line represents the decline expected for ^{56}Co decay.

lines of [O I] $\lambda 5577$, [O I] $\lambda 6300$, 6364, [Ca II] $\lambda 7291$, 7323, and the Ca II NIR triplet emerge and start to dominate the spectra. Na I $\lambda 5890$, 5896, [O I] $\lambda 6300$, 6364, $H\alpha$, and [Ca II] $\lambda 7291$, 7323 all show multipeak profiles after about day 100, as discussed in detail in Section 4.7.

4.2. Comparison with Other SNe II

Fig. 3 compares the spectra of SN 2023ixf with those of other well-studied SNe IIP/L at similar epochs, namely SNe 2013ej⁶ (Valenti et al. 2014; Yuan et al. 2016; Huang et al. 2015), 1999em (Leonard et al. 2002), 2017gmr (Andrews et al. 2019), and 2006ai (Hiramatsu et al. 2021). All spectra were corrected for the redshift, as well as for host-galaxy and Galactic extinctions.

⁶ This previously unpublished spectrum at 337 d is from A. V. Filippenko’s group at UC Berkeley. It was obtained on 26 June 2014 with the DEep Imaging Multi-Object Spectrograph (DEIMOS; Faber et al. 2003) on the 10 m Keck II telescope on Maunakea, with the long slit aligned at the parallactic angle (Filippenko 1982). The spectrum was reduced with standard IRAF routines (Silverman et al. 2012) and was flux calibrated using spectrophotometric standard stars.

As presented in Fig. 3(a), while other comparison SNe have already developed broad P Cygni profiles of the Balmer lines, the spectrum of SN 2023ixf is still characterized by weak flash lines atop a blue continuum. The long-lived narrow flash features indicate that the process of the ejecta engulfing the CSM persists for the first eight days. Such an extended flash-ionization phase is significantly longer compared to the ~ 5 day maximum duration observed in most CCSNe (Bruch et al. 2023), indicating a more radially extended CSM shell around the progenitor and more extensive mass loss before the explosion compared to other cases.

Fig. 3(b) shows a comparison of the spectrum of SN 2023ixf at day 42 with the other SNe at similar phases. SN 2023ixf presents a shallower $H\alpha$ P Cygni absorption than others. Gutiérrez et al. (2014, 2017) found that the smaller ratio of absorption to emission of $H\alpha$ is correlated with brighter and faster declining light curves. The shallower absorption component may imply a deficit in absorbing material at high velocities, which may naturally be reproduced by a rather steep density gradient in the H envelope. A lower envelope mass retained before the explosion may also contribute to the smaller ratio of the absorption to emission of $H\alpha$ (Gutiérrez et al. 2014, 2017; Faran et al.

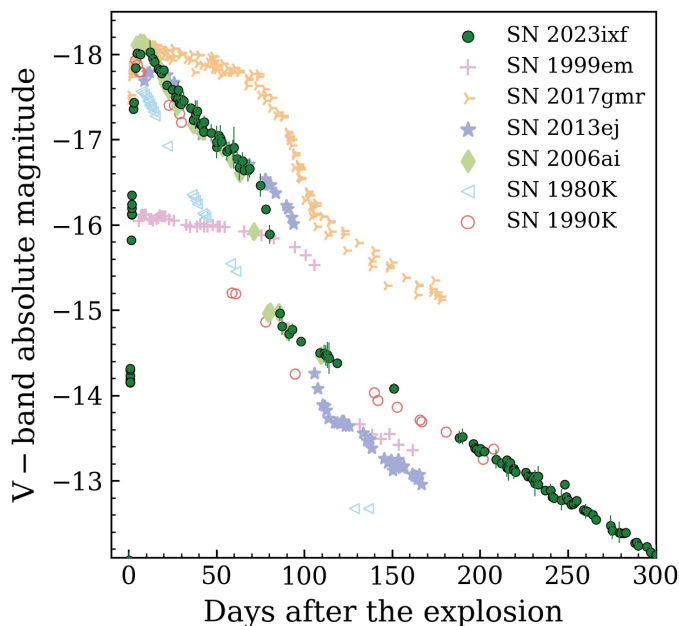


Fig. 2. The absolute V -band light curve of SN2023ixf compared to those of the Type IIP/IIL SNe 1999em (Leonard et al. 2002), 2017gmr (Andrews et al. 2019), 2013ej (Huang et al. 2015), 2006ai (Anderson et al. 2014), 1980K (Buta 1982), and 1990K (Cappellaro et al. 1995). All magnitudes have been corrected for the host and the Galactic extinction components.

2014; Hiramatsu et al. 2021). Hillier & Dessart (2019) proposed that the interaction between the ejecta and CSM could also produce a weak or no $H\alpha$ absorption. In addition, SN 2023ixf has fewer and shallower metal lines than SN 1999em.

Comparison of the day 150 spectrum of SN 2023ixf with those of other SNe is presented in Fig. 3(c). While others still exhibit a P Cygni profile of $H\alpha$, the $H\alpha$ absorption has already disappeared in SN 2023ixf. SN 2023ixf has more prominent [O I] $\lambda\lambda 5577$, [O I] $\lambda\lambda 6300, 6364$, and [Ca II] $\lambda\lambda 7291, 7323$ lines compared to other SNe. The early appearance and strong emission of [O I] may hint that its progenitor was partially stripped before the explosion (Elmhamdi 2011). The Ca II NIR triplet of SN 2023ixf is comparable to that of SN 2017gmr but stronger than that of SN 1999em.

The comparison of the day 328 spectrum is shown in Fig. 3(d). Both SN 2023ixf and SN 2017gmr exhibit a double-peaked [O I] $\lambda\lambda 6300, 6364$ profile, but SN 2013ej has single-peaked [O I]. While the line profiles of SN 2023ixf, SN 2013ej, and SN 2017gmr are overall similar, their light curves show significant differences from each other (Fig. 2).

4.3. Metallicity

The line strengths of some metals measured during the photospheric phase were found to be correlated with the metallicity of their progenitors for SNe IIP/IIL (Dessart et al. 2014). For instance, the pseudo-equivalent width (pEW) of Fe II $\lambda 5018$ can be regarded as a metallicity indicator. The measured pEWs of Fe II $\lambda 5018$ of SN 2023ixf from the spectra between approximately days 50 and 70 and those of the models are presented in Fig. 4. The time interval was chosen to represent the mid-to-

late plateau phase, during which the photosphere still probes the H envelope of the progenitor (Dessart et al. 2014). Without contamination through the outward chemical mixing from the inner core, the strengths of metal lines measured at the outer part of the SN ejecta can reflect the chemical content of the progenitor. As the photosphere of SN 2023ixf recedes into its inner He-rich core after $t \approx 70$ days as indicated by the termination of the plateau phase (Fig. 1), comparison of the observations with the model can be made up to about day 70.

From Fig. 4, one can see that the metallicity of SN 2023ixf falls into the range $(0.4-1)Z_{\odot}$. We remark that one should remain cautious about the inferred range of the metallicity, as the reference models were constructed for SNe IIP with a prominent light-curve plateau, while both the photometric and spectroscopic properties of SN 2023ixf show close resemblances with Type IIL SNe.

4.4. Expansion Velocity

Simulations of SN atmospheres based on the non-LTE CM-FGEN model (Hillier & Miller 1998) suggest that the photospheric velocity of SNe II can be well traced by the absorption minimum of the Fe II $\lambda 5169$ feature (v_{Fe} ; Dessart & Hillier 2005). We measured the absorption minima of Fe II $\lambda 5169$ in SN 2023ixf. At $t \approx 100$ d, the profile of Fe II $\lambda 5169$ no longer follows a Gaussian profile, perhaps owing to line blending, so the velocity is not measured thereafter. The velocity evolution of SN 2023ixf is shown in Fig. 5, together with those measured for the Type IIP SNe 1999em (Takáts & Vinkó 2012) and 2005cs (Takáts & Vinkó 2012), the Type IIP/IIL SN 2013ej (Huang et al. 2015), and the Type II short-plateau SN 2006ai (Hiramatsu et al. 2021).

Comparison of the Fe II $\lambda 5169$ velocity evolution of SN 2023ixf and other Type IIP/L SNe suggests that the former also follows an exponential-like decline as observed in the other presented cases. SN 2023ixf displays an ejecta velocity evolution similar to that measured for SNe 2013ej and 2006ai, significantly higher compared to that of the normal SN IIP 1999em (Elmhamdi et al. 2003; Utrobin et al. 2017) and the subluminous SN IIP 2005cs (Pastorello et al. 2006, 2009). The distinct velocities between subluminous and normal SNe II may be indicative of the associated total energy and the debris of the SN explosion. For example, the former and the latter groups are thought to be linked to the O-Ne-Mg core and Fe core from progenitors with lower ($\sim 8-10 M_{\odot}$) and higher masses ($\geq 10 M_{\odot}$), respectively (Fraser et al. 2011; Janka 2012). Faster expansion velocities of SNe IIP are considered to be linked with higher explosion energies (Dessart et al. 2010; Gutiérrez et al. 2017).

4.5. Distance

The expanding photosphere method (EPM) provides an independent estimate of the distance to a SN based on a comparison between the physical and angular radii of its photosphere, denoted by r and θ , respectively (Kirshner & Kwan 1974). The former can be calculated by multiplying the expansion velocity of the photosphere (v_{phot}) by the time elapsed since the SN explosion ($t - t_0$), and the latter can be used to estimate the distance to the

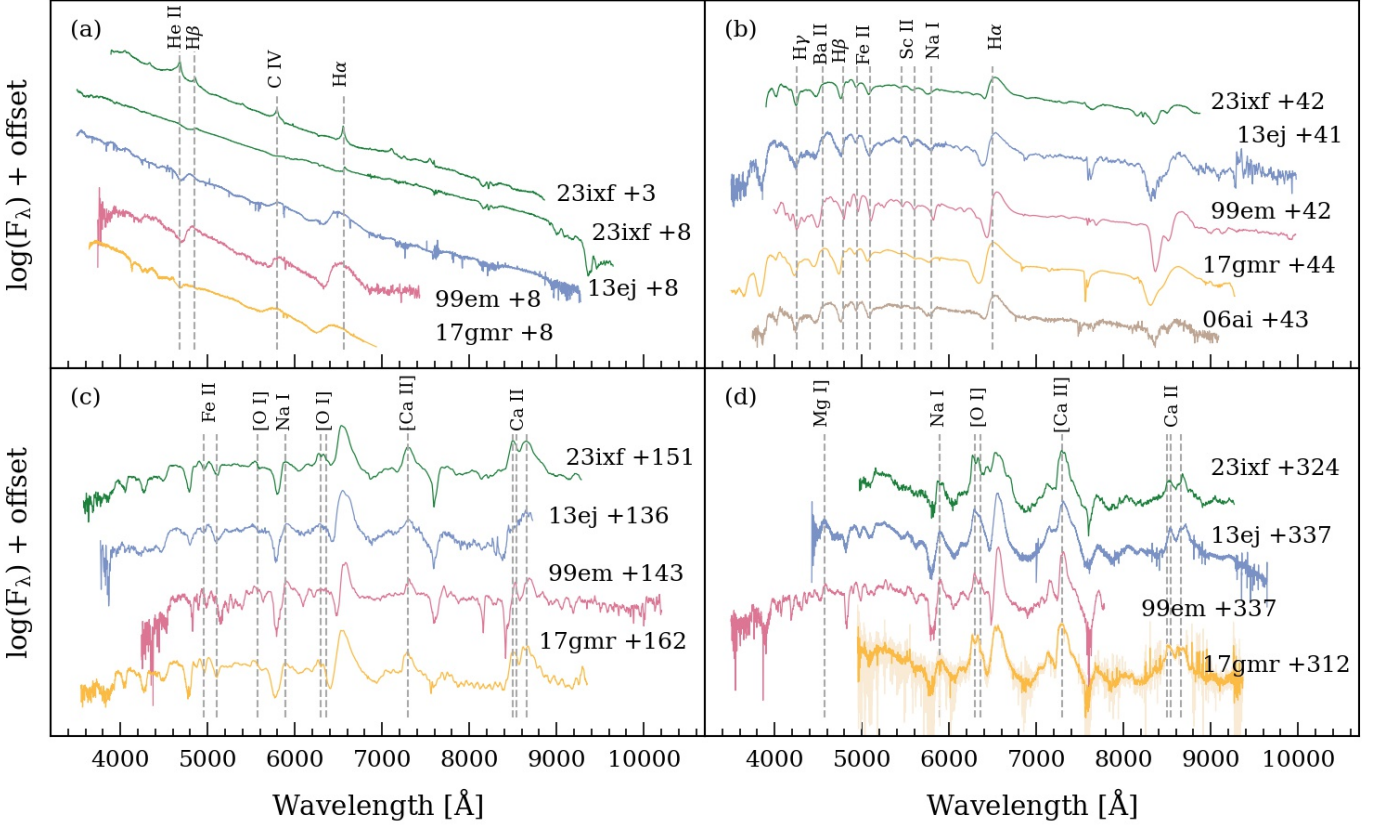


Fig. 3. Spectra of SN 2023ixf at days 5 (a), 40 (b), 151 (c), and 330 (d) compared to that of the Type IIP/L SNe 2013ej (Valenti et al. 2014; Yuan et al. 2016; Huang et al. 2015), 1999em (Leonard et al. 2002), 2017gmr (Andrews et al. 2019) (the spectrum at day 312 is binned, and the original version is plotted with a fainter color), and 2006ai (Hiramatsu et al. 2021) at similar phases. In each panel, major spectral features are marked by vertical dashed lines. For better display, all spectra were shifted arbitrarily and presented with a logarithmic scale.

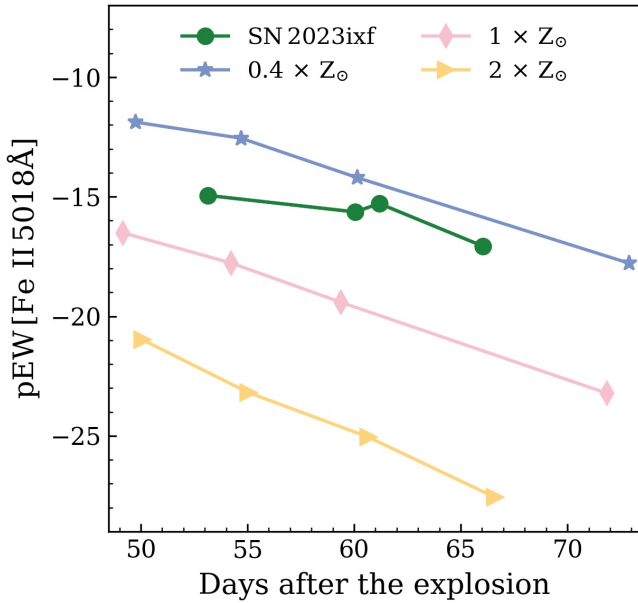


Fig. 4. The pEW of Fe II $\lambda 5018\text{\AA}$ in SN 2023ixf compared with the models presented by Dessart et al. (2014). The 0.4, 1, and $2 \times Z_{\odot}$ models are shown by the color-coded lines (see legend).

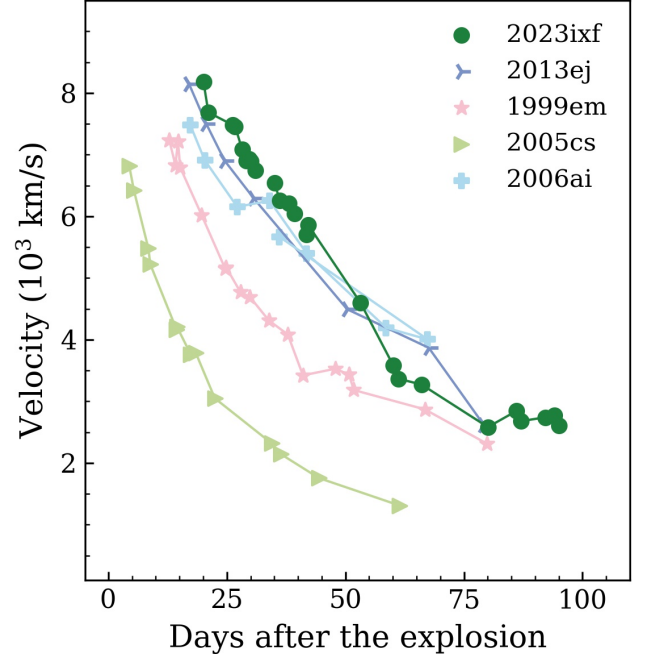


Fig. 5. Comparison of the evolution of the Fe II $\lambda 5169$ velocity of SN 2023ixf with those of SNe 2013ej, 1999em, 2005cs, and 2006ai.

SN (D) through direct geometric calculation,

$$\frac{v_{\text{phot}}(t - t_0)}{D} = \theta.$$

(1) We adopt the velocities measured from the absorption minimum of Fe II $\lambda 5169$ to represent v_{phot} as discussed in Section 4.4.

Following the prescriptions described by Leonard et al. (2002) and Dessart & Hillier (2005), the comparison between the synthetic magnitude calculated from a blackbody spectrum and the photometry of the SN in a given bandpass can be facilitated by minimizing the quantity ϵ , and θ can be derived via

$$\epsilon = \sum_{BVI} \{m_{BVI} - A_{BVI} + 5 \log \theta + 5 \log [\zeta(T_c)] - b_{BVI}(T_c)\}^2, \quad (2)$$

where b_{BVI} is the synthetic broadband magnitude of the Planck function with temperature T_c . The dilution factor ζ corrects the difference between the thermalization and photospheric radii whereas the former is determined by the blackbody temperature (Eastman et al. 1996; Hamuy et al. 2001). We transform the i -band magnitude to Johnson I with the Lupton (2005) color transformations⁷.

Minimization of the quantity ϵ was achieved through a Markov Chain Monte Carlo (MCMC) approach. Upon the determination of θ and v_{phot} , the distance to the SN was then carried out based on Equation 1. The priors of parameters are assumed to be uniform. Jones et al. (2009) show a clear departure from linearity between θ/v versus t after $t \approx 45$ –50 days, likely caused by the progressively emerging spectral lines that deviate the continuum emission of a blackbody (Dessart & Hillier 2005). Therefore, we restricted the EPM analysis to before this phase.

Based on the EPM approach, we estimate the distance to M 101 as $D = 6.35^{+0.31}_{-0.39}$ Mpc ($\mu = 29.01^{+0.10}_{-0.14}$ mag). The distance derived using the standard candle method (Zheng et al. 2025) is 28.67 ± 0.14 mag. Distances measured with Cepheids range from 6.19 to 8.99 Mpc (Mager et al. 2013; Macri et al. 2001), while those measured with SNe Ia range from 5.92 to 7.52 Mpc (Matheson et al. 2012; Munari et al. 2013). Therefore, our result is consistent with distances measured from other methods.

4.6. $H\alpha$ Profile During the Nebular Phase

During the photospheric phase, the $H\alpha$ line of SN 2023ixf is characterized by a P Cygni profile, as shown in Fig. A.1. After $t \approx 90$ days, the absorption component of $H\alpha$ is diminished and the emission component of $H\alpha$ starts to develop into a double-peaked profile. The evolution of the nebular-phase $H\alpha$ profile, normalized by the pseudocontinuum, is shown in Fig. 6 (note that the 407 day spectrum has been published by Zheng et al. (2025)). It is evident that the $H\alpha$ line of SN 2023ixf developed a complex profile when entering the nebular phase. For instance, at $t \approx 189$ days, the profile exhibits a multipeak structure with emission peaks ranging from $\sim -1500 \text{ km s}^{-1}$ (blueshifted) to $\sim +1500 \text{ km s}^{-1}$ (redshifted). The blueshifted component appears stronger than the redshifted counterpart. Such an asymmetric $H\alpha$ profile was also observed in other SNe II, such as SN 1999em (Leonard et al. 2002), SN 2013ej (Huang et al. 2015), and SN 2017gmr (Andrews et al. 2019), and has been attributed to bipolar distribution of Ni.

⁷ <https://www.sdss3.org/dr8/algorithms/sdssUBVRITransform.php#Lupton2005>.

The suppressed redshifted component could instead be attributed to dust formation, as first proposed for the late-time spectral evolution of SN 1987A (Lucy et al. 1989). On-site dust formation has also been reported in some CC-SNe, such as SN 2006jc (Smith et al. 2008), SN 1999em (Elmhamdi et al. 2003), SN 2010jl (Zhang et al. 2012), and SN 2018hfm (Zhang et al. 2022), most likely taking place in a cold dense shell (CDS) between the forward-shock and reverse-shock fronts (Chugai 2001; Chugai et al. 2004; Dessart et al. 2009). In SN 2023ixf, further evidence of dust formation can be inferred from the flux excesses in the NIR and mid-infrared (MIR) light curves taken beyond ~ 120 days (Singh et al. 2024; Van Dyk et al. 2024b). In particular, the MIR light curve displays a prominent brightening at day ~ 210 at $\sim 4.6 \mu\text{m}$, which can be explained by the emergence of line emission from the 1–0 vibrational band of carbon monoxide (CO) at $4.65 \mu\text{m}$.

We also note that starting from $t \approx 90$ days, a notch on the red shoulder of the $H\alpha$ line started to develop, indicating the contribution from a flat-topped component underlying the emission feature (Fig. A.1). As shown by the $t \approx 93$ day spectrum in Fig. 6, the box-shaped continuum extends to a velocity range of ~ 5000 – 8000 km s^{-1} with respect to the rest-frame zero velocity of $H\alpha$. Such a boxy-shaped emission feature provides signatures of strong interaction between the expanding ejecta and shell-like CSM. The edges of the emission indicate the expanding velocity of the ejecta (see, e.g., Dessart & Hillier 2022). Thus, this boxy-shaped emission suggests a CSM shell at a distance of $\sim 6.2 \times 10^{15} \text{ cm}$. Assuming the CSM shell was produced by a typical RSG wind at a velocity of $\sim 10 \text{ km s}^{-1}$, this material was expelled ~ 200 yr before the explosion. A blueshifted peak at $\sim -8000 \text{ km s}^{-1}$ started to emerge at day 190, which shifted gradually to $\sim -5000 \text{ km s}^{-1}$ by $t \approx 400$ days. The different profiles on the right and left sides of $H\alpha$ above 5000 km s^{-1} may naturally be attributed to the presence of a spherically asymmetric dense shell. Furthermore, we note that the shoulder on the right side of the $H\alpha$ profile persisted until day ~ 150 , and emerged again from roughly day 275. This may indicate a persisting interaction with multiple CSM shells. The latter may result from multiple episodes of mass loss that lead to SN 2023ixf at $\gtrsim 200$ yr before the explosion. These bumps might also be attributed to bipolar ejecta at the largest velocity interacting with the CSM (Smith et al. 2012).

The narrow component at 0 km s^{-1} appearing at days 160–189 might be from the host galaxy, as weak [S II] $\lambda\lambda 6716, 6731$ lines are observed at the same epoch.

4.7. Temporal Evolution of the Spectral Line Profiles in the Nebular Phase

For the purpose of investigating the temporal evolution of the morphology of several prominent spectral features in the nebular phase of SN 2023ixf, we normalized the spectra by the pseudocontinuum. Spectral lines of Na I $\lambda\lambda 5890, 5896$, [O I] $\lambda\lambda 6300, 6364$, $H\alpha$, and [Ca II] $\lambda\lambda 7291, 7323$, spanning days 132 to 407, are shown in Fig. 7. We inspect the line velocities of [O I] $\lambda\lambda 6300, 6364$ and [Ca II] $\lambda\lambda 7291, 7323$ with respect to their rest-frame wavelengths.

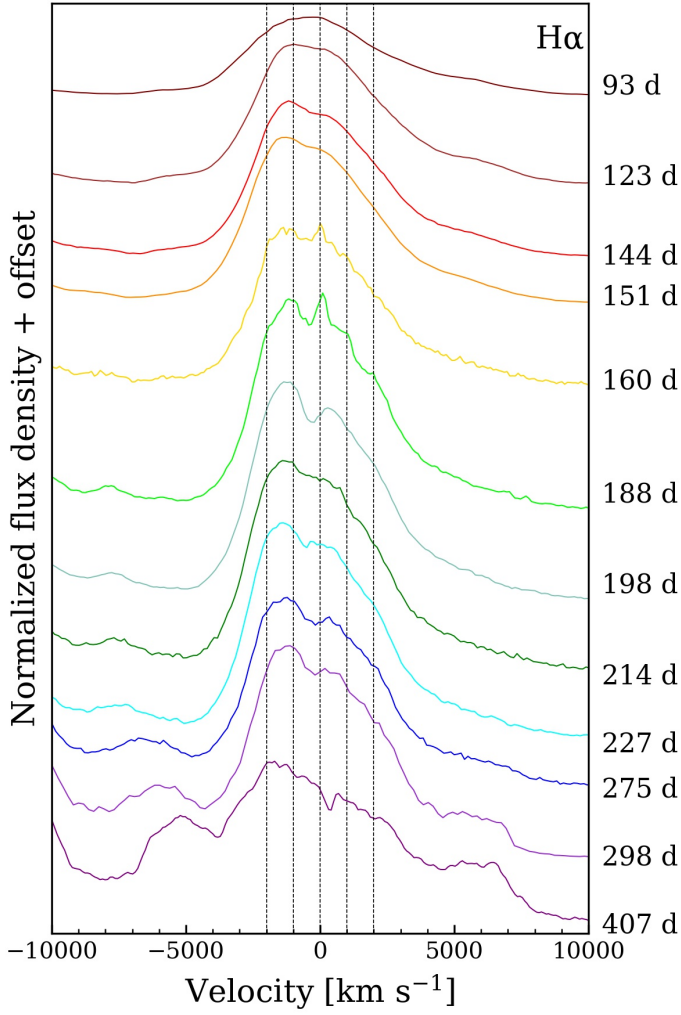


Fig. 6. Temporal evolution of the $H\alpha$ profile from days 93 to 298. Three vertical black dashed lines mark the rest-frame velocities of -2000 , -1000 , 0 , $+1000$ and $+2000$ km s^{-1} , respectively.

First, as the photosphere progressively recedes, the emission component of the $\text{Na I D } \lambda\lambda 5890, 5896$ doublet emerges in the spectra. A double-peaked emission profile centered at zero velocity can be identified, with a nearly constant pEW over time. The blueshifted and redshifted components peak at ~ -1500 and $+1500$ km s^{-1} , respectively. As lines from $[\text{O I}]$ and $[\text{Ca II}]$ strengthen with time with respect to the pseudocontinuum, $H\alpha$ diminishes gradually. Second, the $H\alpha$ line also exhibits a dual-peaked morphology as seen from the $\text{Na I } \lambda\lambda 5890, 5896$ doublet, which also peaked at ~ -1500 and $+1500$ km s^{-1} , respectively. Third, the velocity profiles centered at 6300 and 6364 \AA suggest that both doublets display a blueshifted component at -1500 km s^{-1} . A similar characterization can also be inferred for the $[\text{Ca II}] \lambda\lambda 7291, 7323$ profile. Finally, a redshifted component can be identified from the shoulders in the red-side profiles of the $[\text{Ca II}]$ doublet at a velocity of $\sim +1500$ km s^{-1} . We tentatively identify a redshifted component in the $[\text{O I}]$ lines as they are likely blended with the blue wing of $H\alpha$.

In summary, the zoom-in of the pseudocontinuum-normalized profiles of the presented lines of interest exhibits a more prominent component shifted by ~ 1500 km s^{-1} to the

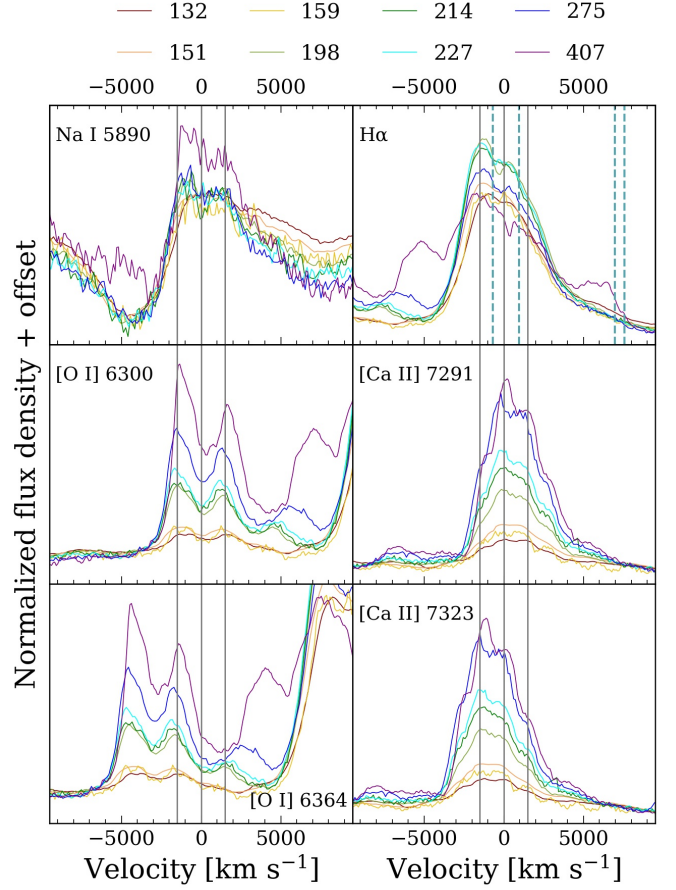


Fig. 7. Temporal evolution of the spectral line profiles centered at the rest-frame wavelengths of $\text{Na I } \lambda\lambda 5890, 5896$, $[\text{O I}] \lambda\lambda 6300, [\text{O I}] \lambda\lambda 6364$, $H\alpha$, $[\text{Ca II}] \lambda\lambda 7291$, and $[\text{Ca II}] \lambda\lambda 7323$ as labeled in each subpanel. All spectra are presented in velocity space. Three vertical black dashed lines mark the rest-frame velocities of -1500 , 0 , and $+1500$ km s^{-1} , respectively. The blue dotted lines mark the $[\text{N II}] \lambda\lambda 6548, 6583$ and $[\text{S II}] \lambda\lambda 6716, 6731$ emission lines from an H II region in the host galaxy.

blue, and another relatively weaker component shifted by ~ 1500 km s^{-1} to the red. The dual-peaked spectral line profiles of SN 2023ixf might hint at an aspherical distribution of the ejecta (Utrobin et al. 2021; Chugai et al. 2005).

4.8. Near-Infrared Spectroscopy

In Figure 8, we present a total of seven NIR spectra of SN 2023ixf obtained with TNG+NICS. At ~ 4 days past explosion, the spectrum exhibits a weak narrow emission line of $P\beta$ 1.282 μm superimposed on the continuum. Seven days later, $P\beta$ disappears and no prominent line can be identified. At ~ 30 days after explosion, $P\beta$ and $B\gamma$ 2.165 μm appear and strengthen over time. $P\beta$ develops a P Cygni profile at 49 d. $\text{Mg I } 1.503$ μm and $\text{Si I } 1.203$ μm appear at about 70 d. $P\alpha$ 1.875 μm is seriously compromised by the telluric absorption. No CO overtone at 2.3 μm is discernible.

We compare the NIR spectra of SN 2023ixf with those of SN 2013ej (Davis et al. 2019) at similar phases (Fig. 9). The narrow $P\beta$ observed in SN 2023ixf at $t \approx 4$ days cannot be discerned in SN 2013ej at $t \approx 5$ days. The spectra of SN 2023ixf show

much stronger and broader Mg I 1.503 μm and Si I 1.203 μm than SN 2013ej.

5. Discussion

5.1. ^{56}Ni mass

^{56}Ni is synthesized during the SN explosion. The trapping of the γ -rays produced in the decay chain $^{56}\text{Ni} \rightarrow ^{56}\text{Co} \rightarrow ^{56}\text{Fe}$ is the main power source of the radioactive-tail luminosity of SNe. Therefore, the bolometric flux of the tail can be utilized to estimate the amount of radioactive ^{56}Ni synthesized in the SN explosion.

During the plateau and post-plateau phases, the V -band light curve of Type II/IIP SNe provides a good proxy for the bolometric evolution. This has been characterized in detail by Bersten & Hamuy (2009), who found a root-mean-square (rms) scatter of ~ 0.11 mag in the difference between the V and bolometric light curves:

$$\log L_t = -0.4[BC + V_t - A(V) - 11.64] + \log_{10}(4\pi D^2), \quad (3)$$

where L_t is the SN luminosity in units of erg s^{-1} when it settles to the radioactive-decay tail, D is the distance in cm, and BC denotes the bolometric correction which has been estimated as -0.70 ± 0.02 (Bersten & Hamuy 2009).

As shown in Fig. 1 and discussed in Section 3, the radioactive tail of SN 2023ixf declines faster than the decay of ^{56}Co assuming full trapping of gamma-ray photons. Therefore, we infer an incomplete trapping of γ -ray photons, which could be attributed to the decreasing photon diffusion time as the SN ejecta expand and become more transparent. Accounting for the γ -ray leakage, the luminosity from solely the $^{56}\text{Ni} \rightarrow ^{56}\text{Co} \rightarrow ^{56}\text{Fe}$ decay chain can be fitted following the prescription of Yuan et al. (2016):

$$L = 1.41 \times 10^{43} m_{\text{Ni}} (e^{-t/t_{\text{Co}}} - e^{-t/t_{\text{Ni}}})(1 - e^{t_1^2/t^2}), \quad (4)$$

where L is the bolometric luminosity, m_{Ni} gives the mass of ^{56}Ni synthesized in the SN explosion, t represents the time since explosion, and t_{Co} and t_{Ni} are the e -folding times of ^{56}Co and ^{56}Ni (111.4 and 8.8 days, respectively). The term t_1 represents the characteristic time when the γ -ray optical depth of the ejecta drops to unity. This characteristic timescale is determined by the average γ -ray opacity, the total mass of the ejecta, and the kinetic energy of the SN. The t^{-2} dependence of the optical depth is due to the decreasing column density as the SN ejecta undergo homologous expansion (Clocchiatti & Wheeler 1997).

We therefore adopt Equation 3 to convert the V -band photometry of SN 2023ixf between days 90 and 350 to the bolometric light curve and estimate the mass of ^{56}Ni synthesized in the ejecta by fitting Equation 4 assuming incomplete trapping of X-rays and electrons/positrons. The best fit to the single radioactive decay chain model suggests $m_{\text{Ni}} = 0.059 \pm 0.001 M_{\odot}$ and $t_1 = 312.9 \pm 4.6$ days. The derived Ni mass is consistent with that calculated by Singh et al. (2024). The estimated Ni mass of SN 2023ixf is higher than that of SN 1999em, which is $0.02 M_{\odot}$ (Elmhamdi et al. 2003).

5.2. Comparison of Nebular Spectra with Theoretical Models

While the SN expands, its deep interior becomes visible as a result of decreased column densities and removal of free electrons owing to recombination. Spectra at the nebular phase are hence free from photospheric absorption lines and are typically dominated by emission features. Nebular-phase spectra of CC-SNe thus reveal the physical conditions of a variety of nuclear burning zones, enabling unambiguous model diagnostics.

In Figure 10, we compare the $t \approx 275$ day spectrum of SN 2023ixf with a set of theoretical models with ZAMS masses of 12, 15, and 19 M_{\odot} at similar phases (at $t \approx 250$ day; Jerkstrand et al. 2014). The spectrum of SN 2023ixf is flux calibrated using interpolated photometry. For comparison purposes, all spectra have been scaled with respect to the total flux integrated over the observed wavelength range. We note that the profile of the [O I] $\lambda\lambda 6300, 6364$ doublet of SN 2023ixf is in good agreement with that calculated for the 15 M_{\odot} to 19 M_{\odot} models. However, the [Ca II] $\lambda\lambda 7291, 7323$ doublet of SN 2023ixf is a little bit stronger than that of the models, and $H\alpha$ of SN 2023ixf is much weaker than the modeled profiles. Note that the $H\alpha$, [Ca II] $\lambda\lambda 7291, 7323$, and Ca II NIR triplet are mainly formed in the outer layers of the H-rich ejecta. Consequently, their line strengths are dependent on both the pre-explosion mass loss and the distribution of the associated elements themselves. The latter may indicate the degree of outward mixing of Ni-rich ejecta.

5.3. Progenitor Mass Estimation

In particular, being one of the products of a series of hydrostatic burning phases, the amount of oxygen in the ejecta increases with ZAMS mass. Since oxygen also acts as the fuel for calcium production during the explosive burning phase, the flux ratio of [O I] $\lambda\lambda 6300, 6364$ to [Ca II]/[O I] provides a sensitive indicator of the ZAMS mass of the progenitor of CC-SNe (Fransson & Chevalier 1989; Jerkstrand et al. 2012, 2014, 2015). Our spectra of SN 2023ixf have been scaled to match the photometry at different bandpasses. The photometry is interpolated or extrapolated to get the corresponding values at the phases the spectra were taken. The spectrum at day 298 is constructed from the spectra taken on days 297.2 and 298.1.

To derive the progenitor mass of SN 2023ixf, we first estimate the continuum underlying the [O I] line by connecting the visually inspected blue end of the [O I] and the red end of $H\alpha$. This “pseudocontinuum” represented by such a line segment is then subtracted from the spectral region of interest, as shown in Fig. B.1. Second, a multicomponent Gaussian function is used to fit the features of the [O I] + $H\alpha$ emission complex between days 275 and 407. For the measurement of each phase, we calculate the area below the Gaussian functions that fit the $\lambda\lambda 6300, 6364$ feature to obtain the [O I] luminosity. Finally, we divide the time series of [O I] luminosity by the intensity integrated in the range 4800–8900 \AA of the same spectrum. The aim of the last step of normalization is to remove the dependence of [O I] luminosity on the γ -ray trapping. The selected wavelength range is similar to that adopted by Anderson et al. (2018); Fang et al. (2024).

In Figure 11, we present the fraction of the [O I] flux of SN 2023ixf at days 275, 298, and 407. The same calculation was

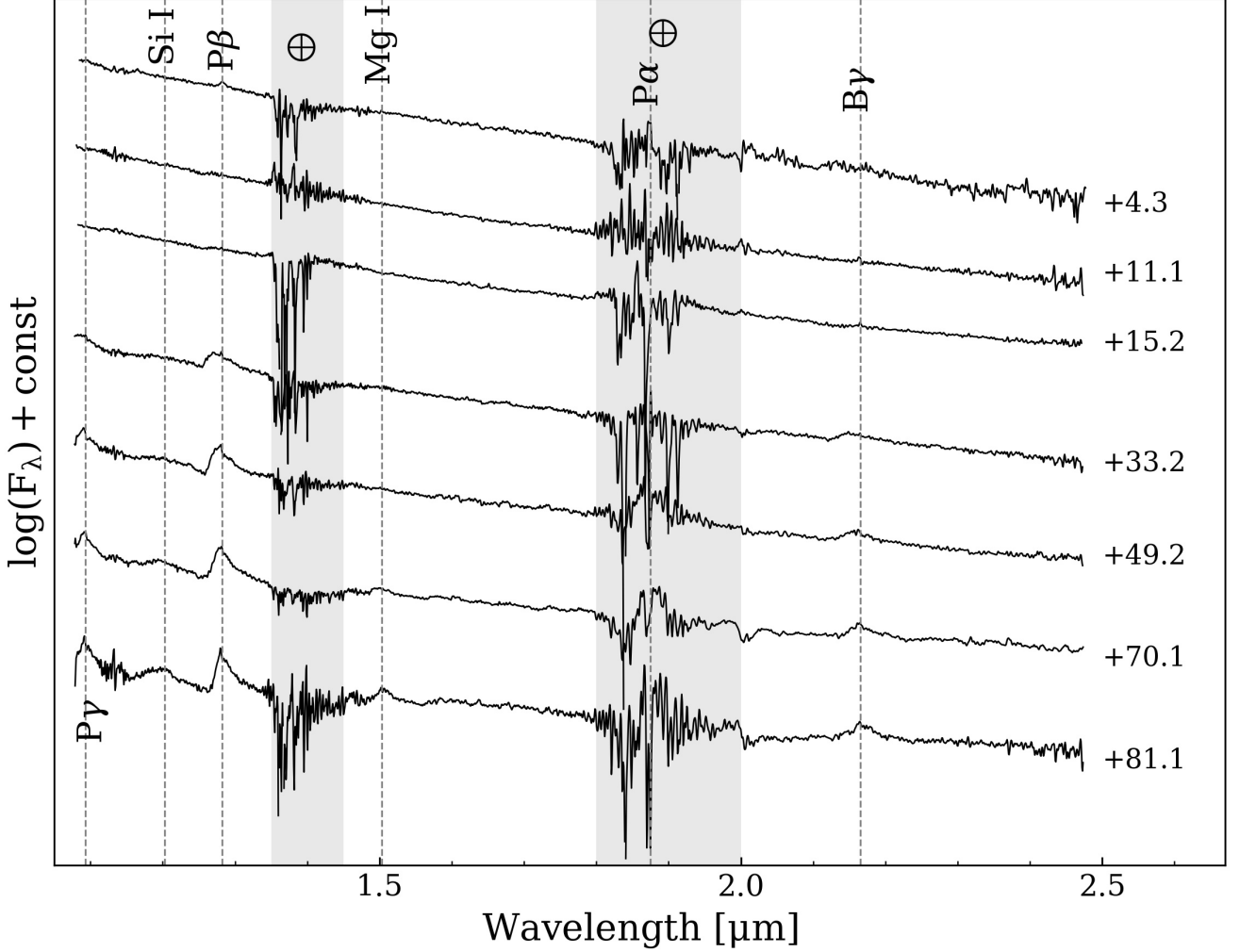


Fig. 8. NIR spectra of SN 2023ixf observed by TNG from $t \approx 4$ to 80 days after the explosion. Phases are indicated to the right of each spectrum. Several prominent spectral lines are marked with vertical dashed lines. Telluric lines are shown by crossed circles and gray shade.

also carried out for a series of model spectra with different progenitor ZAMS masses as computed by Jerkstrand et al. (2014). The [O I] percentages of SN 2023ixf estimated in the nebular phase fall in the progenitor mass range of 15–19 M_{\odot} , consistent with the results of Fang et al. (2024); Jencson et al. (2023); Niu et al. (2023); Qin et al. (2024); Zheng et al. (2025).

We remark that the [O I] flux estimated based on multicomponent Gaussian fitting may introduce additional systematic uncertainties that are difficult to characterize. For example, any departure from spherical symmetry would alter the shape of the line profile. Additionally, dust formation may alter the line asymmetry by suppressing the flux in the blue wing and creating an extended profile in the red wing. A box-shaped underlying continuum of H α blended with [O I] may affect the estimation of the flux of [O I]. However, as the measurements of the data and the models were carried out following an identical procedure, and the intensity-normalized [O I] flux measured for various progenitor models confirms the trend of increasing mass of the progenitor, we suggest that the ZAMS mass estimated for SN 2023ixf based on the [O I] flux remains robust.

6. Conclusion

We present extensive optical and NIR photometric and spectroscopic observations of SN 2023ixf spanning 3–625 days after the explosion. The narrow flash lines of SN 2023ixf persist for the first eight days. These long-lived features indicate a radially extended CSM shell around the progenitor. SN 2023ixf reaches a V-band absolute peak magnitude of $M_V = -18.1 \pm 0.1$ mag about 6 days after the explosion, which is toward the bright end of Type II SNe. SN 2023ixf presents a slanted plateau phase (~ 1.47 mag per 100 d in V), indicating a less massive H envelope than those of normal Type IIP SNe.

The photospheric velocities of SN 2023ixf are higher than those of typical SNe IIP, suggesting higher ejecta kinetic energy. The metallicity of SN 2023ixf derived from the pEW of Fe II during the photospheric phase falls between $0.4 Z_{\odot}$ and $1 Z_{\odot}$. Using EPM, we estimate the distance to the SN as $6.35^{+0.31}_{-0.39}$ Mpc.

Taking into account the incomplete trapping of the γ -rays, we use the radioactive-tail luminosity of SN 2023ixf to calculate the mass of ^{56}Ni synthesized during the SN explosion. The derived mass is $0.059 \pm 0.001 M_{\odot}$. We compare the percentage of [O I] flux with that of the synthetic spectra in Jerkstrand et al.

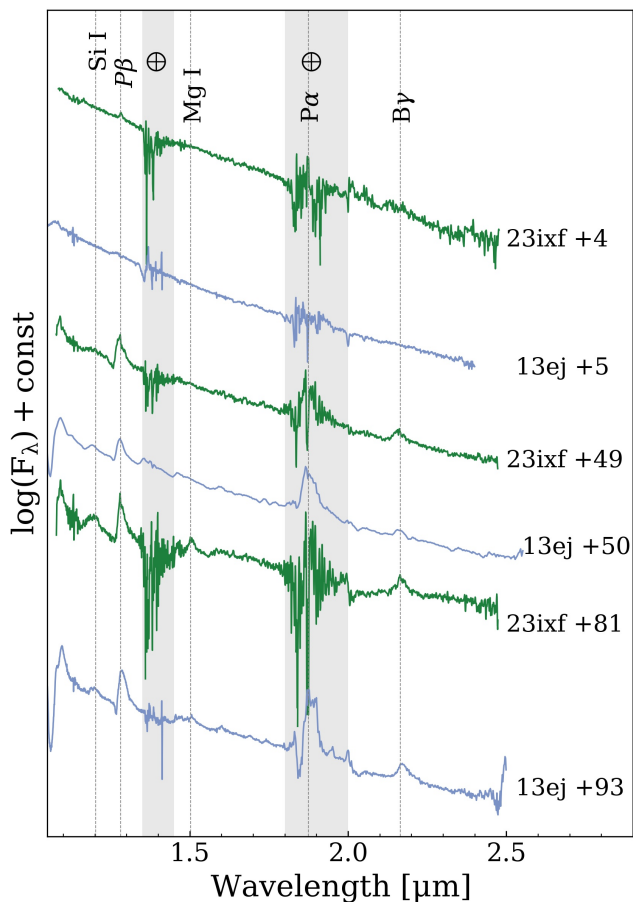


Fig. 9. Comparison of the NIR spectra of SN 2023ixf with those of SN 2013ej at similar phases. Several prominent spectral features are marked by dashed lines, and telluric absorption is shown by crossed circles and gray shade.

(2014); the derived progenitor mass of SN 2023ixf is 15–19 M_{\odot} , consistent with the results suggested from *HST* and *Spitzer* archival images. The emission lines of hydrogen, sodium, oxygen, and calcium exhibit double-peaked profiles during the nebular phase, hinting at an aspherical distribution of the ejecta. The box-shaped $H\alpha$ profile extending up to 8000 km s⁻¹ indicates interaction between the ejecta and CSM. The different profiles on the blue and red sides of the $H\alpha$ profile may be attributed to a spherically asymmetric CSM shell. The disappearance of the red shoulder of $H\alpha$ at day \sim 150 and its reappearance at day \sim 275 might result from multiple episodes of mass loss \gtrsim 200 yr before the explosion.

7. Acknowledgments

This work is supported by the National Science Foundation of China (NSFC grants 12288102 and 12033003) and the Tencent Xplorer Prize. A.R. acknowledges financial support from the GRAWITA Large Program Grant (PI P. D’Avanzo) and from PRIN-INAF 2022 “Shedding light on the nature of gap transients: from the observations to the models.” Y.-Z. Cai is supported by NSFC grant 12303054, the National Key Research and Development Program of China (grant 2024YFA1611603), the Yunnan Fundamental Research Projects (grant 202401AU070063), and the International Centre of Su-

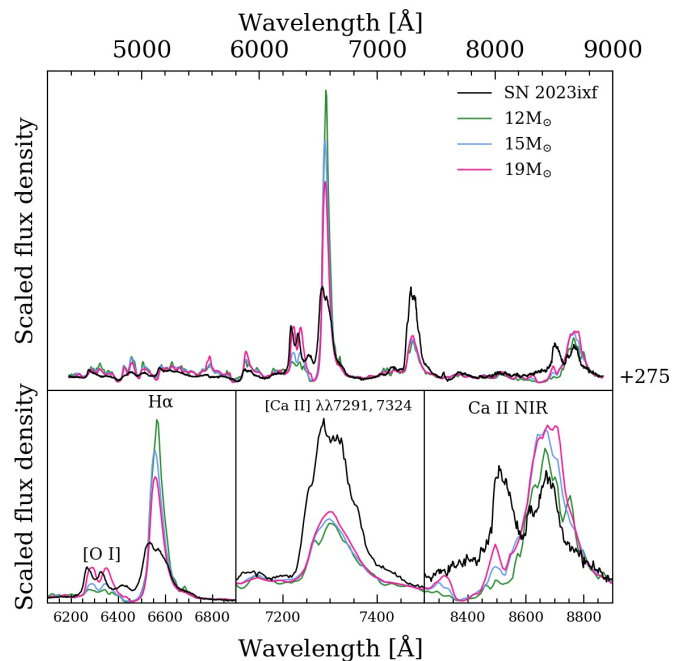


Fig. 10. Comparison between the nebular-phase spectrum of SN 2023ixf obtained at day 275 and the NLTE model spectra at day 250 for CCSNe with ZAMS mass of 12, 15, and 19 M_{\odot} . The subpanels in the lower row zoom in on the [O I] + $H\alpha$, [Ca II], and Ca II NIR triplet regions.

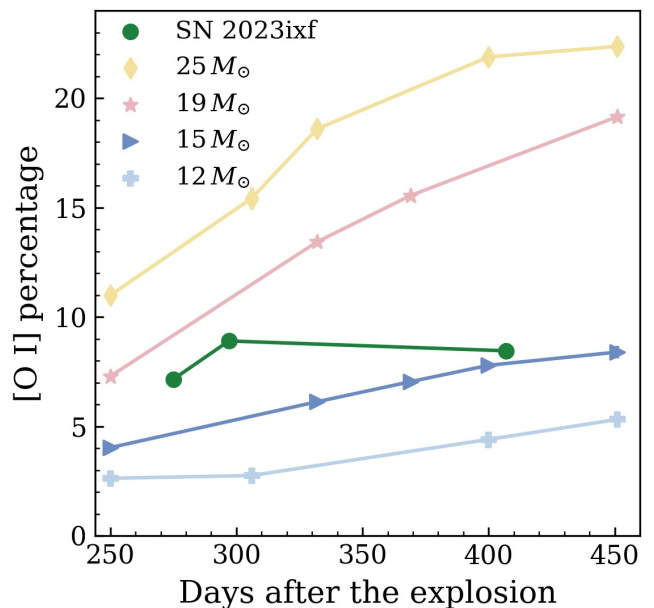


Fig. 11. The temporal evolution of the measured [O I] $\lambda\lambda$ 6300, 6364 flux for SN 2023ixf as a percentage of the total optical flux, along with that of the modeled spectra presented by Jerkstrand et al. (2014).

pernovae, Yunnan Key Laboratory (grant 202302AN360001). A.P., A.R., G.V., and I.S. are supported by PRIN-INAF 2022 project “Shedding light on the nature of gap transients: from the observations to the models.” J.Z. is supported by the National Key R&D Program of China with grant 2021YFA1600404,

NSFC grants 12173082 and 12333008, the Yunnan Fundamental Research Projects (grants 202501AV070012, 202401BC070007 and 202201AT070069), the Top-notch Young Talents Program of Yunnan Province, the Light of West China Program provided by the Chinese Academy of Sciences, and the International Centre of Supernovae, Yunnan Key Laboratory (grant 202302AN360001). M.H. acknowledges the support from the Postdoctoral Fellowship Program of CPSF under Grant Number GZB20240376, and the Shuimu Tsinghua Scholar Program 2024SM118. A.V.F.'s group at UC Berkeley is grateful for financial support from the Christopher R. Redlich Fund, Gary and Cynthia Bengier, Clark and Sharon Winslow, Sanford Robertson (Y.Y. was a Bengier-Winslow-Robertson Postdoctoral Fellow when this work was started), and many other donors.

We acknowledge the support of the staff of the Xinglong 80cm telescope and the Xinglong 2.16m telescope. This work was partially supported by the Open Project Program of the Key Laboratory of Optical Astronomy, National Astronomical Observatories, Chinese Academy of Sciences.

Some of the data presented herein were obtained at the W. M. Keck Observatory, which is operated as a scientific partnership among the California Institute of Technology, the University of California, and NASA; the observatory was made possible by the generous financial support of the W. M. Keck Foundation. We thank Melissa Graham, Patrick Kelly, WeiKang Zheng, and Jon Mauerhan for assistance obtaining the Keck SN 2013ej spectrum.

References

- Ahumada, R., Allende Prieto, C., Almeida, A., et al. 2020, *ApJS*, 249, 3, doi: 10.3847/1538-4365/ab929e
- Anderson, J. P., González-Gaitán, S., Hamuy, M., et al. 2014, *ApJ*, 786, 67, doi: 10.1088/0004-637X/786/1/67
- Anderson, J. P., Dessart, L., Gutiérrez, C. P., et al. 2018, *Nature Astronomy*, 2, 574, doi: 10.1038/s41550-018-0458-4
- Andrews, J. E., Sand, D. J., Valenti, S., et al. 2019, *ApJ*, 885, 43, doi: 10.3847/1538-4357/ab43e3
- Arcavi, I., Gal-Yam, A., Cenko, S. B., et al. 2012, *ApJ*, 756, L30, doi: 10.1088/2041-8205/756/2/L30
- Baffa, C., Comoretto, G., Gennari, S., et al. 2001, *A&A*, 378, 722, doi: 10.1051/0004-6361:20011194
- Barbieri, C., Bhatia, R. K., Bonoli, C., et al. 1994, in *Society of Photo-Optical Instrumentation Engineers (SPIE) Conference Series*, Vol. 2199, *Advanced Technology Optical Telescopes V*, ed. L. M. Stepp, 10–21, doi: 10.1117/12.176189
- Barbon, R., Ciatti, F., & Rosino, L. 1979, *A&A*, 72, 287
- Baron, E., Branch, D., Hauschildt, P. H., et al. 2000, *ApJ*, 545, 444, doi: 10.1086/317795
- Bersten, M. C., & Hamuy, M. 2009, *ApJ*, 701, 200, doi: 10.1088/0004-637X/701/1/200
- Bose, S., Sutarra, F., Kumar, B., et al. 2015, *ApJ*, 806, 160, doi: 10.1088/0004-637X/806/2/160
- Bostroem, K. A., Pearson, J., Shrestha, M., et al. 2023, *ApJ*, 956, L5, doi: 10.3847/2041-8213/acf9a4
- Brennan, S. J., & Fraser, M. 2022, *A&A*, 667, A62, doi: 10.1051/0004-6361/202243067
- Bruch, R. J., Gal-Yam, A., Schulze, S., et al. 2021, *ApJ*, 912, 46, doi: 10.3847/1538-4357/abef05
- Bruch, R. J., Gal-Yam, A., Yaron, O., et al. 2023, *ApJ*, 952, 119, doi: 10.3847/1538-4357/acd8be
- Burrows, A., & Vartanyan, D. 2021, *Nature*, 589, 29, doi: 10.1038/s41586-020-03059-w
- Burrows, A., Wang, T., & Vartanyan, D. 2024, *ApJ*, 964, L16, doi: 10.3847/2041-8213/ad319e
- Buta, R. J. 1982, *PASP*, 94, 578, doi: 10.1086/131026
- Cappellaro, E., Danziger, I. J., della Valle, M., Gouiffes, C., & Turatto, M. 1995, *A&A*, 293, 723
- Chugai, N. N. 2001, *MNRAS*, 326, 1448, doi: 10.1111/j.1365-2966.2001.04717.x
- Chugai, N. N., Fabrika, S. N., Sholukhova, O. N., et al. 2005, *Astronomy Letters*, 31, 792, doi: 10.1134/1.2138766
- Chugai, N. N., Blinnikov, S. I., Cumming, R. J., et al. 2004, *MNRAS*, 352, 1213, doi: 10.1111/j.1365-2966.2004.08011.x
- Clocchiatti, A., & Wheeler, J. C. 1997, *ApJ*, 491, 375, doi: 10.1086/304961
- Davis, S., Hsiao, E. Y., Ashall, C., et al. 2019, *ApJ*, 887, 4, doi: 10.3847/1538-4357/ab4c40
- de Jaeger, T., Zheng, W., Stahl, B. E., et al. 2019, *MNRAS*, 490, 2799, doi: 10.1093/mnras/stz2714
- Dessart, L., & Hillier, D. J. 2005, *A&A*, 439, 671, doi: 10.1051/0004-6361:20053217
- . 2022, *A&A*, 660, L9, doi: 10.1051/0004-6361/202243372
- Dessart, L., Hillier, D. J., Gezari, S., Basa, S., & Matheson, T. 2009, *MNRAS*, 394, 21, doi: 10.1111/j.1365-2966.2008.14042.x
- Dessart, L., Livne, E., & Waldman, R. 2010, *MNRAS*, 408, 827, doi: 10.1111/j.1365-2966.2010.17190.x
- Dessart, L., Gutierrez, C. P., Hamuy, M., et al. 2014, *MNRAS*, 440, 1856, doi: 10.1093/mnras/stu417
- Eastman, R. G., Schmidt, B. P., & Kirshner, R. 1996, *ApJ*, 466, 911, doi: 10.1086/177563
- Ehgamberdiev, S. 2018, *Nature Astronomy*, 2, 349, doi: 10.1038/s41550-018-0459-3
- Elmhamdi, A. 2011, *Acta Astron.*, 61, 179, doi: 10.48550/arXiv.1109.2318
- Elmhamdi, A., Danziger, I. J., Chugai, N., et al. 2003, *MNRAS*, 338, 939, doi: 10.1046/j.1365-8711.2003.06150.x
- Faber, S. M., Phillips, A. C., Kibrick, R. I., et al. 2003, in *Society of Photo-Optical Instrumentation Engineers (SPIE) Conference Series*, Vol. 4841, *Instrument Design and Performance for Optical/Infrared Ground-based Telescopes*, ed. M. Iye & A. F. M. Moorwood, 1657–1669, doi: 10.1117/12.460346

- Fan, Y.-F., Bai, J.-M., Zhang, J.-J., et al. 2015, *Research in Astronomy and Astrophysics*, 15, 918, doi: [10.1088/1674-4527/15/6/014](#)
- Fang, Q., Moriya, T. J., Ferrari, L., et al. 2024, arXiv e-prints, arXiv:2409.03540, doi: [10.48550/arXiv.2409.03540](#)
- Faran, T., Poznanski, D., Filippenko, A. V., et al. 2014, *MNRAS*, 445, 554, doi: [10.1093/mnras/stu1760](#)
- Ferrari, L., Folatelli, G., Ertini, K., Kuncarayakti, H., & Andrews, J. E. 2024, *A&A*, 687, L20, doi: [10.1051/0004-6361/202450440](#)
- Filippenko, A. V. 1982, *PASP*, 94, 715, doi: [10.1086/131052](#)
- Folatelli, G., Ferrari, L., Ertini, K., Kuncarayakti, H., & Maeda, K. 2025, arXiv e-prints, arXiv:2502.10534, doi: [10.48550/arXiv.2502.10534](#)
- Fransson, C., & Chevalier, R. A. 1989, *ApJ*, 343, 323, doi: [10.1086/167707](#)
- Fraser, M., Ergon, M., Eldridge, J. J., et al. 2011, *MNRAS*, 417, 1417, doi: [10.1111/j.1365-2966.2011.19370.x](#)
- Fukugita, M., Ichikawa, T., Gunn, J. E., et al. 1996, *AJ*, 111, 1748, doi: [10.1086/117915](#)
- Gal-Yam, A., Arcavi, I., Ofek, E. O., et al. 2014, *Nature*, 509, 471, doi: [10.1038/nature13304](#)
- Gutiérrez, C. P., Anderson, J. P., Hamuy, M., et al. 2014, *ApJ*, 786, L15, doi: [10.1088/2041-8205/786/2/L15](#)
- . 2017, *ApJ*, 850, 90, doi: [10.3847/1538-4357/aa8f42](#)
- Hamuy, M., Pinto, P. A., Maza, J., et al. 2001, *ApJ*, 558, 615, doi: [10.1086/322450](#)
- Henden, A. A., Templeton, M., Terrell, D., et al. 2016, *VizieR Online Data Catalog: AAVSO Photometric All Sky Survey (APASS) DR9 (Henden+, 2016), VizieR On-line Data Catalog: II/336. Originally published in: 2015AAS...22533616H*
- Hillier, D. J., & Dessart, L. 2019, *A&A*, 631, A8, doi: [10.1051/0004-6361/201935100](#)
- Hillier, D. J., & Miller, D. L. 1998, *ApJ*, 496, 407, doi: [10.1086/305350](#)
- Hiramatsu, D., Howell, D. A., Moriya, T. J., et al. 2021, *ApJ*, 913, 55, doi: [10.3847/1538-4357/abf6d6](#)
- Hiramatsu, D., Tsuna, D., Berger, E., et al. 2023, *ApJ*, 955, L8, doi: [10.3847/2041-8213/acf299](#)
- Huang, F., Li, J.-Z., Wang, X.-F., et al. 2012, *Research in Astronomy and Astrophysics*, 12, 1585, doi: [10.1088/1674-4527/12/11/012](#)
- Huang, F., Wang, X., Zhang, J., et al. 2015, *ApJ*, 807, 59, doi: [10.1088/0004-637X/807/1/59](#)
- Itagaki, K. 2023, *Transient Name Server Discovery Report*, 2023-1158, 1
- Janka, H.-T. 2012, *Annual Review of Nuclear and Particle Science*, 62, 407, doi: [10.1146/annurev-nucl-102711-094901](#)
- Janka, H.-T., Melson, T., & Summa, A. 2016, *Annual Review of Nuclear and Particle Science*, 66, 341, doi: [10.1146/annurev-nucl-102115-044747](#)
- Jenson, J. E., Pearson, J., Beasor, E. R., et al. 2023, *ApJ*, 952, L30, doi: [10.3847/2041-8213/ace618](#)
- Jerkstrand, A. 2017, in *Handbook of Supernovae*, ed. A. W. Alsabti & P. Murdin, 795, doi: [10.1007/978-3-319-21846-5_29](#)
- Jerkstrand, A., Ergon, M., Smartt, S. J., et al. 2015, *A&A*, 573, A12, doi: [10.1051/0004-6361/201423983](#)
- Jerkstrand, A., Fransson, C., Maguire, K., et al. 2012, *A&A*, 546, A28, doi: [10.1051/0004-6361/201219528](#)
- Jerkstrand, A., Smartt, S. J., Fraser, M., et al. 2014, *MNRAS*, 439, 3694, doi: [10.1093/mnras/stu221](#)
- Johnson, H. L., Mitchell, R. I., Iriarte, B., & Wisniewski, W. Z. 1966, *Communications of the Lunar and Planetary Laboratory*, 4, 99
- Jones, M. I., Hamuy, M., Lira, P., et al. 2009, *ApJ*, 696, 1176, doi: [10.1088/0004-637X/696/2/1176](#)
- Khokhlov, A. M., Höflich, P. A., Oran, E. S., et al. 1999, *ApJ*, 524, L107, doi: [10.1086/312305](#)
- Kilpatrick, C. D., Foley, R. J., Jacobson-Galán, W. V., et al. 2023, *ApJ*, 952, L23, doi: [10.3847/2041-8213/ace4ca](#)
- Kirshner, R. P., & Kwan, J. 1974, *ApJ*, 193, 27, doi: [10.1086/153123](#)
- Kumar, A., Dastidar, R., Maund, J. R., Singleton, A. J., & Sun, N.-C. 2025, *MNRAS*, 538, 659, doi: [10.1093/mnras/staf312](#)
- Landolt, A. U. 1992, *AJ*, 104, 340, doi: [10.1086/116242](#)
- Lang, D., Hogg, D. W., Mierle, K., Blanton, M., & Roweis, S. 2010, *AJ*, 139, 1782, doi: [10.1088/0004-6256/139/5/1782](#)
- LeBlanc, J. M., & Wilson, J. R. 1970, *ApJ*, 161, 541, doi: [10.1086/150558](#)
- Leonard, D. C., Filippenko, A. V., Gates, E. L., et al. 2002, *PASP*, 114, 35, doi: [10.1086/324785](#)
- Li, G., Hu, M., Li, W., et al. 2024, *Nature*, 627, 754, doi: [10.1038/s41586-023-06843-6](#)
- Li, W., Leaman, J., Chornock, R., et al. 2011, *MNRAS*, 412, 1441, doi: [10.1111/j.1365-2966.2011.18160.x](#)
- Lucy, L. B., Danziger, I. J., Gouffes, C., & Bouchet, P. 1989, in *IAU Colloq. 120: Structure and Dynamics of the Interstellar Medium*, ed. G. Tenorio-Tagle, M. Moles, & J. Melnick, Vol. 350, 164, doi: [10.1007/BFb0114861](#)
- Macri, L. M., Calzetti, D., Freedman, W. L., et al. 2001, *ApJ*, 549, 721, doi: [10.1086/319465](#)
- Maeda, K., & Nomoto, K. 2003, *ApJ*, 598, 1163, doi: [10.1086/378948](#)
- Mager, V. A., Madore, B. F., & Freedman, W. L. 2013, *ApJ*, 777, 79, doi: [10.1088/0004-637X/777/1/79](#)
- Matheson, T., Joyce, R. R., Allen, L. E., et al. 2012, *ApJ*, 754, 19, doi: [10.1088/0004-637X/754/1/19](#)
- Michel, P. D., Mazzali, P. A., Perley, D. A., Hinds, K. R., & Wise, J. L. 2025, *MNRAS*, doi: [10.1093/mnras/staf443](#)
- Mösta, P., Ott, C. D., Radice, D., et al. 2015, *Nature*, 528, 376, doi: [10.1038/nature15755](#)
- Munari, U., Henden, A., Belligoli, R., et al. 2013, *New A*, 20, 30, doi: [10.1016/j.newast.2012.09.003](#)
- Nakar, E., & Sari, R. 2010, *ApJ*, 725, 904, doi: [10.1088/0004-637X/725/1/904](#)
- Niu, Z., Sun, N.-C., Maund, J. R., et al. 2023, *ApJ*, 955, L15, doi: [10.3847/2041-8213/acf4e3](#)
- Obergaulinger, M., Janka, H. T., & Aloy, M. A. 2014, *MNRAS*, 445, 3169, doi: [10.1093/mnras/stu1969](#)
- Pastorello, A., Sauer, D., Taubenberger, S., et al. 2006, *MNRAS*, 370, 1752, doi: [10.1111/j.1365-2966.2006.10587.x](#)
- Pastorello, A., Valentí, S., Zampieri, L., et al. 2009, *MNRAS*, 394, 2266, doi: [10.1111/j.1365-2966.2009.14505.x](#)
- Perley, D., & Gal-Yam, A. 2023, *Transient Name Server Classification Report*, 2023-1164, 1
- Pledger, J. L., & Shara, M. M. 2023, *ApJ*, 953, L14, doi: [10.3847/2041-8213/ace88b](#)
- Popov, D. V. 1993, *ApJ*, 414, 712, doi: [10.1086/173117](#)
- Poznanski, D., Prochaska, J. X., & Bloom, J. S. 2012, *MNRAS*, 426, 1465, doi: [10.1111/j.1365-2966.2012.21796.x](#)
- Qin, Y.-J., Zhang, K., Bloom, J., et al. 2024, *MNRAS*, 534, 271, doi: [10.1093/mnras/stae2012](#)
- Quimby, R. M., Wheeler, J. C., Höflich, P., et al. 2007, *ApJ*, 666, 1093, doi: [10.1086/520532](#)
- Riess, A. G., Yuan, W., Macri, L. M., et al. 2022, *ApJ*, 934, L7, doi: [10.3847/2041-8213/ac5c5b](#)
- Sanders, N. E., Soderberg, A. M., Gezari, S., et al. 2015, *ApJ*, 799, 208, doi: [10.1088/0004-637X/799/2/208](#)
- Schlafly, E. F., & Finkbeiner, D. P. 2011, *ApJ*, 737, 103, doi: [10.1088/0004-637X/737/2/103](#)
- Schlegel, E. M. 1990, *MNRAS*, 244, 269
- Silverman, J. M., Foley, R. J., Filippenko, A. V., et al. 2012, *MNRAS*, 425, 1789, doi: [10.1111/j.1365-2966.2012.21270.x](#)
- Singh, A., Teja, R. S., Moriya, T. J., et al. 2024, *ApJ*, 975, 132, doi: [10.3847/1538-4357/ad7955](#)
- Skrutskie, M. F., Cutri, R. M., Stiening, R., et al. 2006, *AJ*, 131, 1163, doi: [10.1086/498708](#)
- Smartt, S. J. 2009, *ARA&A*, 47, 63, doi: [10.1146/annurev-astro-082708-101737](#)
- . 2015, *PASA*, 32, e016, doi: [10.1017/pasa.2015.17](#)
- Smartt, S. J., Eldridge, J. J., Crockett, R. M., & Maund, J. R. 2009, *MNRAS*, 395, 1409, doi: [10.1111/j.1365-2966.2009.14506.x](#)
- Smith, N. 2017, in *Handbook of Supernovae*, ed. A. W. Alsabti & P. Murdin, 403, doi: [10.1007/978-3-319-21846-5_38](#)
- Smith, N., Foley, R. J., & Filippenko, A. V. 2008, *ApJ*, 680, 568, doi: [10.1086/587860](#)
- Smith, N., Pearson, J., Sand, D. J., et al. 2023, *ApJ*, 956, 46, doi: [10.3847/1538-4357/acf366](#)
- Smith, N., Cenko, S. B., Butler, N., et al. 2012, *MNRAS*, 420, 1135, doi: [10.1111/j.1365-2966.2011.20104.x](#)
- Soker, N. 2016, *New A Rev.*, 75, 1, doi: [10.1016/j.newar.2016.08.002](#)
- Soraisam, M. D., Szalai, T., Van Dyk, S. D., et al. 2023, *ApJ*, 957, 64, doi: [10.3847/1538-4357/acef22](#)
- Takáts, K., & Vinkó, J. 2012, *MNRAS*, 419, 2783, doi: [10.1111/j.1365-2966.2011.19921.x](#)
- Teja, R. S., Singh, A., Basu, J., et al. 2023, *ApJ*, 954, L12, doi: [10.3847/2041-8213/acf620](#)

- Tody, D. 1986, in Society of Photo-Optical Instrumentation Engineers (SPIE) Conference Series, Vol. 627, Instrumentation in astronomy VI, ed. D. L. Crawford, 733, doi: 10.1117/12.968154
- Tody, D. 1993, in Astronomical Society of the Pacific Conference Series, Vol. 52, Astronomical Data Analysis Software and Systems II, ed. R. J. Hanisch, R. J. V. Brissenden, & J. Barnes, 173
- Utrobin, V. P., Wongwathanarat, A., Janka, H. T., & Müller, E. 2017, *ApJ*, 846, 37, doi: 10.3847/1538-4357/aa8594
- Utrobin, V. P., Chugai, N. N., Andrews, J. E., et al. 2021, *MNRAS*, 505, 116, doi: 10.1093/mnras/stab1369
- Valenti, S., Sand, D., Pastorello, A., et al. 2014, *MNRAS*, 438, L101, doi: 10.1093/mnrasl/s1t171
- Van Dyk, S. D., Srinivasan, S., Andrews, J. E., et al. 2024a, *ApJ*, 968, 27, doi: 10.3847/1538-4357/ad414b
- Van Dyk, S. D., Szalai, T., Cutri, R. M., et al. 2024b, arXiv e-prints, arXiv:2406.18005, doi: 10.48550/arXiv.2406.18005
- Vartanyan, D., Tsang, B. T. H., Kasen, D., et al. 2024, arXiv e-prints, arXiv:2411.03434, doi: 10.48550/arXiv.2411.03434
- Vasylyev, S. S., Yang, Y., Filippenko, A. V., et al. 2023, *ApJ*, 955, L37, doi: 10.3847/2041-8213/acf1a3
- Wang, C.-J., Bai, J.-M., Fan, Y.-F., et al. 2019, *Research in Astronomy and Astrophysics*, 19, 149, doi: 10.1088/1674-4527/19/10/149
- Wang, T., & Burrows, A. 2024, *ApJ*, 969, 74, doi: 10.3847/1538-4357/ad5009
- Woosley, S. E., Langer, N., & Weaver, T. A. 1995, *ApJ*, 448, 315, doi: 10.1086/175963
- Xiang, D., Mo, J., Wang, L., et al. 2024, *Science China Physics, Mechanics, and Astronomy*, 67, 219514, doi: 10.1007/s11433-023-2267-0
- Yang, Y., Baade, D., Hoefflich, P., et al. 2023, *MNRAS*, 519, 1618, doi: 10.1093/mnras/stac3477
- Yaron, O., Perley, D. A., Gal-Yam, A., et al. 2017, *Nature Physics*, 13, 510, doi: 10.1038/nphys4025
- Yuan, F., Jerkstrand, A., Valenti, S., et al. 2016, *MNRAS*, 461, 2003, doi: 10.1093/mnras/stw1419
- Zampieri, L., Pastorello, A., Turatto, M., et al. 2003, *MNRAS*, 338, 711, doi: 10.1046/j.1365-8711.2003.06082.x
- Zhang, J., Lin, H., Wang, X., et al. 2023, *Science Bulletin*, 68, 2548, doi: 10.1016/j.scib.2023.09.015
- Zhang, J.-C., Fan, Z., Yan, J.-Z., et al. 2016a, *PASP*, 128, 105004, doi: 10.1088/1538-3873/128/968/105004
- Zhang, K., Wang, X., Zhang, J., et al. 2016b, *ApJ*, 820, 67, doi: 10.3847/0004-637X/820/1/67
- Zhang, T., Wang, X., Wu, C., et al. 2012, *AJ*, 144, 131, doi: 10.1088/0004-6256/144/5/131
- Zhang, X., Wang, X., Sai, H., et al. 2022, *MNRAS*, 509, 2013, doi: 10.1093/mnras/stab3007
- Zheng, W., Dessart, L., Filippenko, A. V., et al. 2025, arXiv e-prints, arXiv:2503.13974, doi: 10.48550/arXiv.2503.13974
- Zimmerman, E. A., Irani, I., Chen, P., et al. 2024, *Nature*, 627, 759, doi: 10.1038/s41586-024-07116-6
- ¹⁰ CISAS G. Colombo, University of Padova, via Venezia 15, 35131, Padova Italy
- ¹¹ UNESCO Chair "Environment, Resources and Sustainable Development", Department of Science and Technology, Parthenope University of Naples, Italy
- ¹² INAF, Osservatorio Astronomico di Capodimonte, Salita Moiariello, 16, Naples, I-80131, Italy
- ¹³ Max-Planck-Institut für Astrophysik, Karl-Schwarzschild Straße 1, 85748 Garching, Germany
- ¹⁴ Beijing Planetarium, Beijing Academy of Sciences and Technology, Beijing 100044, China
- ¹⁵ University of Chinese Academy of Sciences, Beijing 100049, China
- ¹⁶ Ulugh Beg Astronomical Institute, Astronomy Street 33, Tashkent 100052, Uzbekistan
- ¹⁷ National University of Uzbekistan, Tashkent 100174, Uzbekistan
- ¹⁸ School of Space Science and Technology, Shandong University, Weihai, Shandong 264209, China
- ¹⁹ Xingming Observatory, Urumqi, 830000, China
- ²⁰ National Astronomical Observatories, Chinese Academy of Sciences, Beijing 100101, People's Republic of China

¹ Department of Physics, Tsinghua University, Beijing, 100084, China.

² Department of Astronomy, University of California, Berkeley, CA 94720-3411, USA

³ INAF - Osservatorio Astronomico di Padova, Vicolo dell'Osservatorio 5, 35122 Padova, Italy

⁴ INAF - Osservatorio Astronomico di Brera, Via E. Bianchi 46, 23807 Merate (LC), Italy

⁵ Dipartimento di Fisica e Astronomia, Università Degli Studi di Padova, 35121 Padova PD, Italy

⁶ Yunnan Observatories, Chinese Academy of Sciences, Kunming 650216, China

⁷ International Centre of Supernovae, Yunnan Key Laboratory, Kunming 650216, China

⁸ Key Laboratory for the Structure and Evolution of Celestial Objects, Chinese Academy of Sciences, Kunming 650216, China

⁹ INAF-Osservatorio Astronomico di Capodimonte, Salita Moiariello 16, 80131 Napoli, Italy

Appendix A: Spectroscopic observations

Table A.1. Log of optical spectroscopic observations of SN 2023ixf

UTC time (yyyy-mm-dd hh:mm)	MJD	Phase (d)	Range (Å)	Resolution (blue/red)(Å)	Telescope/Instrument
2023-05-21 13:54	60085.58	2.79	3895-8871	4.45	XLT/BFOSC
2023-05-26 12:49	60090.53	7.75	3894-8870	4.45	XLT/BFOSC
2023-05-31 12:39	60095.53	12.74	3892-8869	4.45	XLT/BFOSC
2023-06-01 13:01	60096.54	13.75	3889-8867	4.45	XLT/BFOSC
2023-06-07 20:31	60102.86	20.07	4250-6590	3.6	GT/B&C
2023-06-08 21:00	60103.88	21.09	3320-7890	5.8	GT/B&C
2023-06-09 00:45	60104.03	21.24	3320-7890	5.6	GT/B&C
2023-06-12 02:12	60107.09	24.30	3660-6060	4.1	GT/B&C
2023-06-14 01:34	60109.07	26.28	3320-7890	5.6	GT/B&C
2023-06-15 23:45	60110.99	28.20	3320-7890	5.6	GT/B&C
2023-06-16 22:17	60111.93	29.14	3320-7890	5.7	GT/B&C
2023-06-17 21:01	60112.88	30.09	3320-7890	5.5	GT/B&C
2023-06-18 20:43	60113.83	31.05	3320-7890	5.6	GT/B&C
2023-06-21 16:56	60116.71	33.92	6004-8264	1.79	XLT/BFOSC
2023-06-21 17:29	60116.73	33.94	3900-8875	4.45	XLT/BFOSC
2023-06-22 21:37	60118.90	36.11	4250-6590	3.4	GT/B&C
2023-06-24 13:09	60119.55	36.76	5995-8255	1.79	XLT/BFOSC
2023-06-24 13:40	60119.57	36.78	3913-8890	4.45	XLT/BFOSC
2023-06-25 20:36	60120.86	38.07	3320-7890	5.5	GT/B&C
2023-06-27 00:45	60122.03	39.24	4460-6860	3.7	GT/B&C
2023-06-27 13:45	60122.57	39.79	3936-8921	4.45	XLT/BFOSC
2023-06-27 14:05	60122.59	39.80	3427-5470	1.98	XLT/BFOSC
2023-06-27 14:36	60122.61	39.82	6006-8268	1.79	XLT/BFOSC
2023-06-29 14:13	60124.59	41.80	3905-8885	4.45	XLT/BFOSC
2023-06-29 22:07	60124.92	42.13	3320-7890	5.5	GT/B&C
2023-06-30 14:42	60125.61	42.83	6006-8267	1.79	XLT/BFOSC
2023-07-01 20:59	60126.88	44.09	5775-6975	1.3	GT/B&C
2023-07-10 22:50	60135.95	53.16	3670-6070	4.1	GT/B&C
2023-07-17 20:11	60142.84	60.05	3310-7890	6.9	GT/B&C
2023-07-18 23:33	60143.98	61.19	3310-7890	7.3	GT/B&C
2023-07-23 20:11	60148.84	66.05	3310-7890	6.7	GT/B&C
2023-07-26 14:53	60151.62	68.83	3800-8750	2.85	LJT/YFOSC
2023-08-06 20:02	60162.83	80.05	3310-7890	7.1	GT/B&C
2023-08-12 20:07	60168.84	86.05	3310-7890	6.9	GT/B&C
2023-08-13 19:54	60169.83	87.04	3310-7890	6.6	GT/B&C
2023-08-18 21:22	60174.91	92.12	3320-7890	6.9	GT/B&C
2023-08-19 21:02	60175.88	93.09	4000-9300	14.7	Copernico/AFOSC
2023-08-19 22:10	60175.92	93.14	3320-7890	7.0	GT/B&C
2023-08-20 21:31	60176.90	94.11	3320-7890	6.9	GT/B&C
2023-08-21 20:50	60177.87	95.08	3320-7890	7.2	GT/B&C
2023-08-24 20:25	60180.85	98.06	4250-6590	3.3	GT/B&C
2023-08-31 19:08	60187.80	105.01	3320-7890	7.5	GT/B&C
2023-09-01 20:51	60188.87	106.08	3320-7890	6.8	GT/B&C
2023-09-06 19:14	60193.80	111.01	3320-7890	7.4	GT/B&C
2023-09-08 20:00	60195.83	113.05	5775-6975	1.5	GT/B&C
2023-09-18 11:11	60205.47	122.68	3899-8876	4.45	XLT/BFOSC
2023-09-24 19:08	60211.80	129.01	3320-7890	7.1	GT/B&C
2023-09-27 11:37	60214.48	131.70	3939-8918	4.45	XLT/BFOSC
2023-09-28 20:05	60215.84	133.05	3320-7890	6.2	GT/B&C
2023-09-29 19:11	60216.80	134.01	3320-7890	6.1	GT/B&C
2023-10-06 18:19	60223.76	140.98	4580-7000	3.4	GT/B&C

Continued

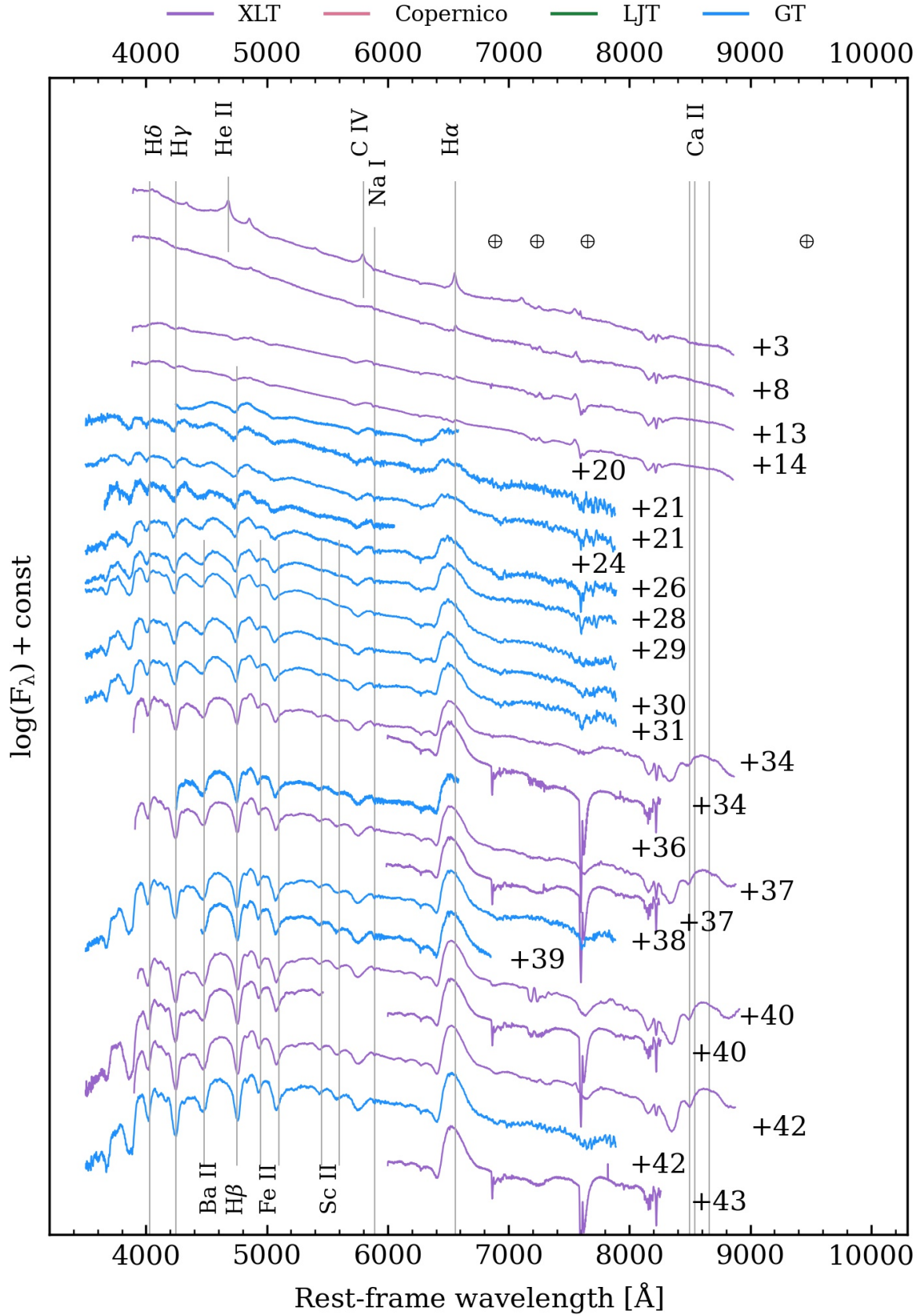
Table A.1 – Continued

UT time (yyyy-mm-dd hh:mm)	MJD	Phase (d)	Range (Å)	Resolution (blue/red)(Å)	Telescope/Instrument
2023-10-09 10:53	60226.45	143.67	3939-8921	4.45	XLT/BFOSC
2023-10-09 18:00	60226.75	143.96	3320-7890	7.3	GT/B&C
2023-10-11 10:38	60228.44	145.66	6006-8275	1.79	XLT/BFOSC
2023-10-11 18:05	60228.75	145.97	3320-7890	7.2	GT/B&C
2023-10-16 18:11	60233.76	150.97	3530-9290	21.6/23.1	Copernico/AFOSC
2023-10-19 10:27	60236.44	153.65	3943-8922	4.45	XLT/BFOSC
2023-10-22 17:27	60239.73	156.94	3320-7890	6.4	GT/B&C
2023-10-25 04:38	60242.19	159.41	3320-7890	5.7	GT/B&C
2023-10-28 17:45	60245.74	162.95	3330-7890	6.5	GT/B&C
2023-11-05 17:11	60253.72	170.93	3320-7890	6.65	GT/B&C
2023-11-11 04:43	60259.20	176.41	3320-7890	5.7	GT/B&C
2023-11-19 04:16	60267.18	184.39	3250-9280	15.4/14.5	Copernico/AFOSC
2023-11-22 04:26	60270.18	187.40	5775-6975	2.1	GT/B&C
2023-11-23 04:19	60271.18	188.39	3320-7890	7.4	GT/B&C
2023-11-29 03:30	60277.15	194.36	5775-6975	2.5	GT/B&C
2023-12-02 21:13	60280.88	198.10	3775-8918	4.45	XLT/BFOSC
2023-12-03 03:28	60281.14	198.36	3315-7888	7.5	GT/B&C
2023-12-07 02:11	60285.09	202.30	4980-9280	23	Copernico/AFOSC
2023-12-16 03:53	60294.16	211.37	5775-6975	2.4	GT/B&C
2023-12-17 01:33	60295.07	212.28	4980-9280	15	Copernico/AFOSC
2023-12-18 21:10	60296.88	214.09	3778-8919	4.45	XLT/BFOSC
2023-12-21 04:56	60299.21	216.42	4890-7305	5.4	GT/B&C
2023-12-31 20:54	60309.87	227.08	3774-8913	4.45	XLT/BFOSC
2024-01-04 04:40	60313.19	230.41	5775-6975	2.7	GT/B&C
2024-01-13 03:21	60322.14	239.35	5775-6975	3.6	GT/B&C
2024-01-16 02:10	60325.09	242.30	3320-7890	6.5	GT/B&C
2024-02-17 21:06	60357.88	275.09	3800-8750	2.85	LJT/YFOSC
2024-03-10 22:59	60379.96	297.17	4000-9300	14.7	Copernico/AFOSC
2024-03-11 21:30	60380.90	298.11	3600-7300	24.5	Copernico/AFOSC
2024-04-07 01:00	60407.04	324.25	4000-9300	14.7	Copernico/AFOSC

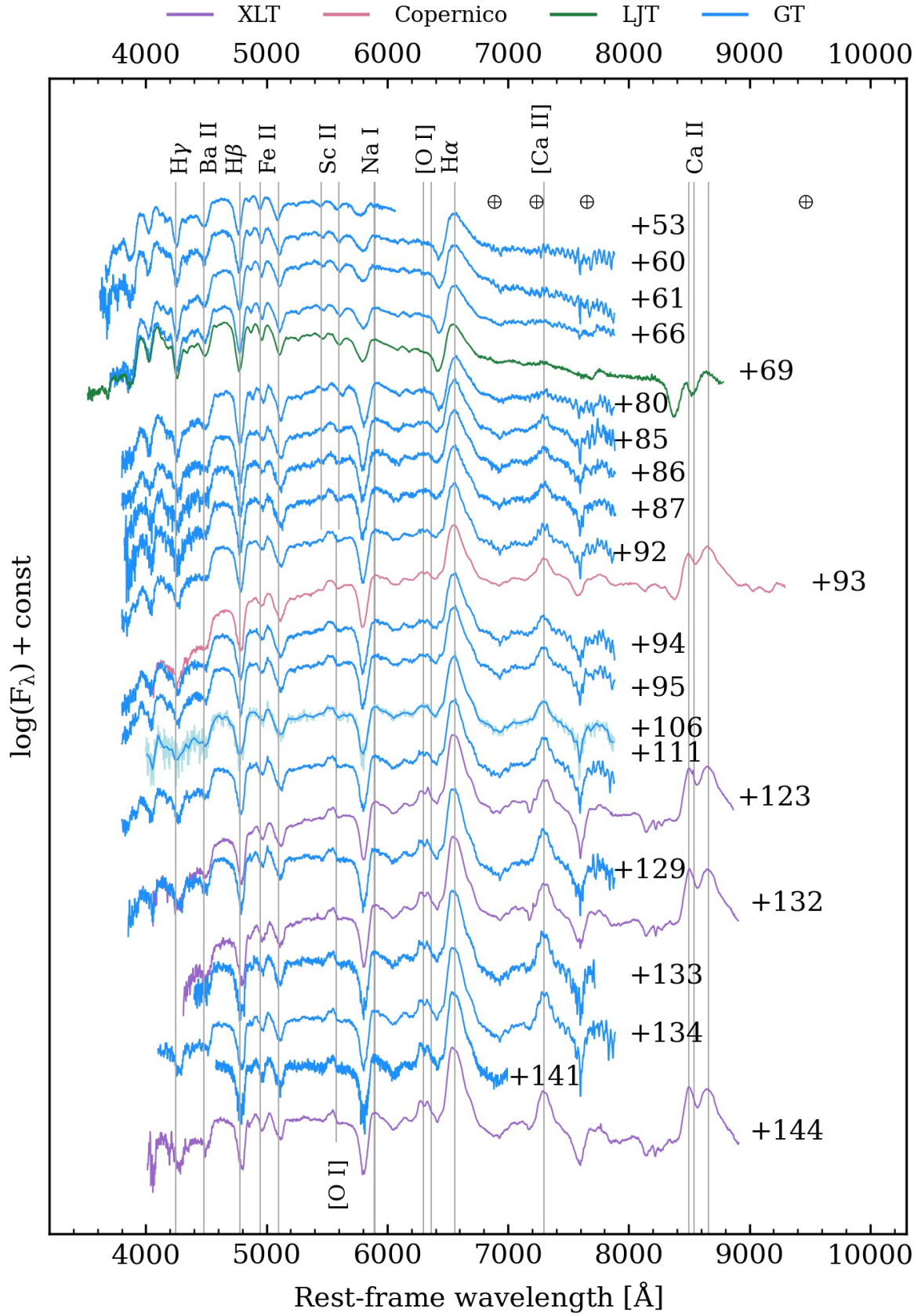
Table A.2. Log of NIR spectroscopic observations of SN 2023ixf

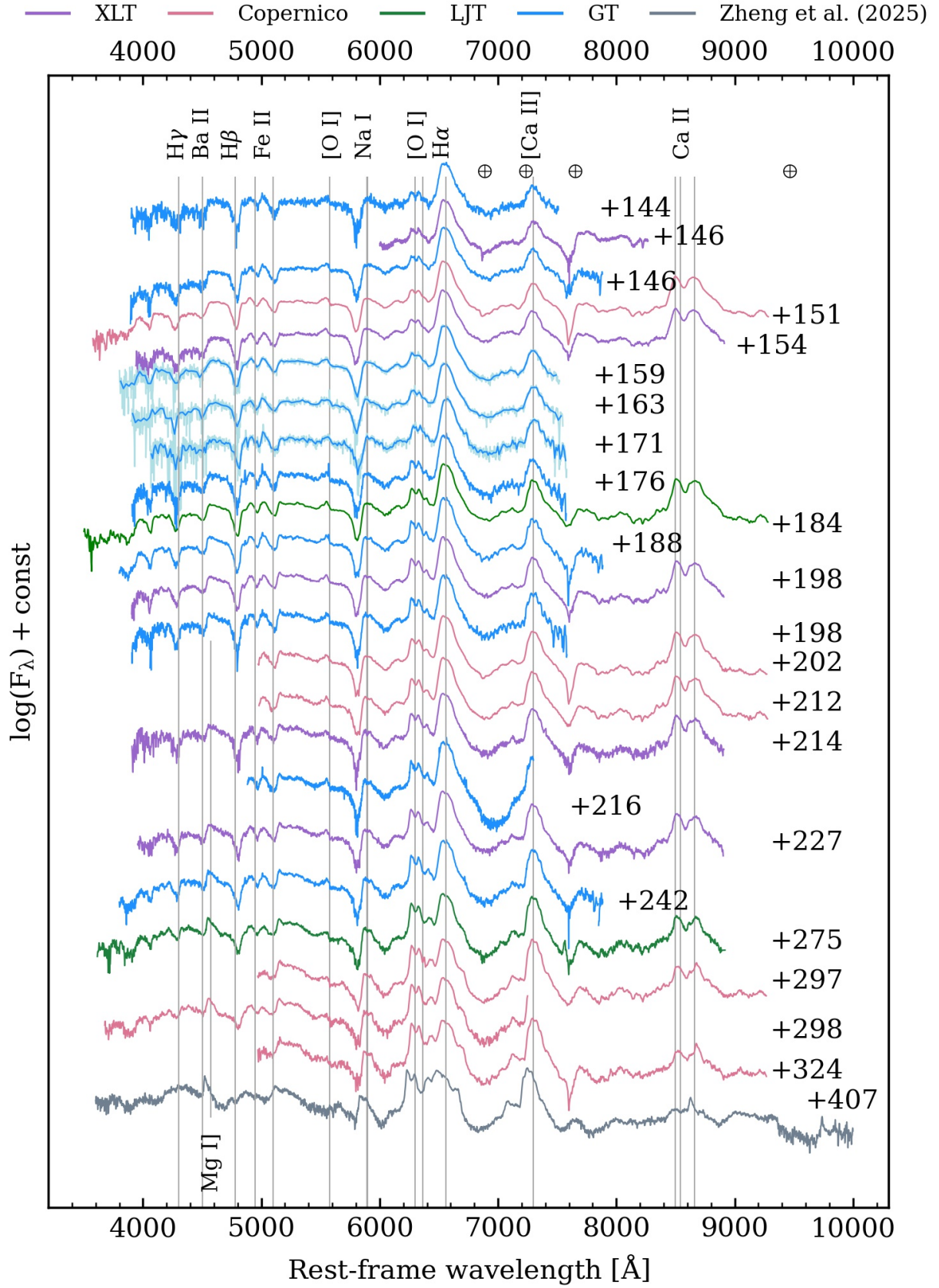
UTC time (yyyy-mm-dd hh:mm)	MJD	Phase (d)	Range (Å)	Resolution (blue/red)(Å)	Telescope/Instrument
2023-05-23 01:50	60087.08	4.29	10850-24776	6.6/11.2	TNG/NICS
2023-05-29 21:16	60093.89	11.10	10807-24743	6.6/11.2	TNG/NICS
2023-06-02 23:04	60097.96	15.17	10830-24721	6.6/11.2	TNG/NICS
2023-06-20 23:09	60115.97	33.18	10783-24735	6.6/11.2	TNG/NICS
2023-07-06 22:58	60131.96	49.17	10781-24735	6.6/11.2	TNG/NICS
2023-07-27 21:33	60152.90	70.11	10784-24743	6.6/11.2	TNG/NICS
2023-08-07 20:55	60163.87	81.08	10788-24741	6.6/11.2	TNG/NICS

Fig. A.1. Spectral time series of SN2023ixf spanning days 3 to 324. Observations conducted with different instruments are color coded and distinguished by the legend at the top. Phases are marked on the right. Some major telluric lines are identified by \oplus . Some noisy spectra are binned, with the original version plotted with a fainter color.



Continued





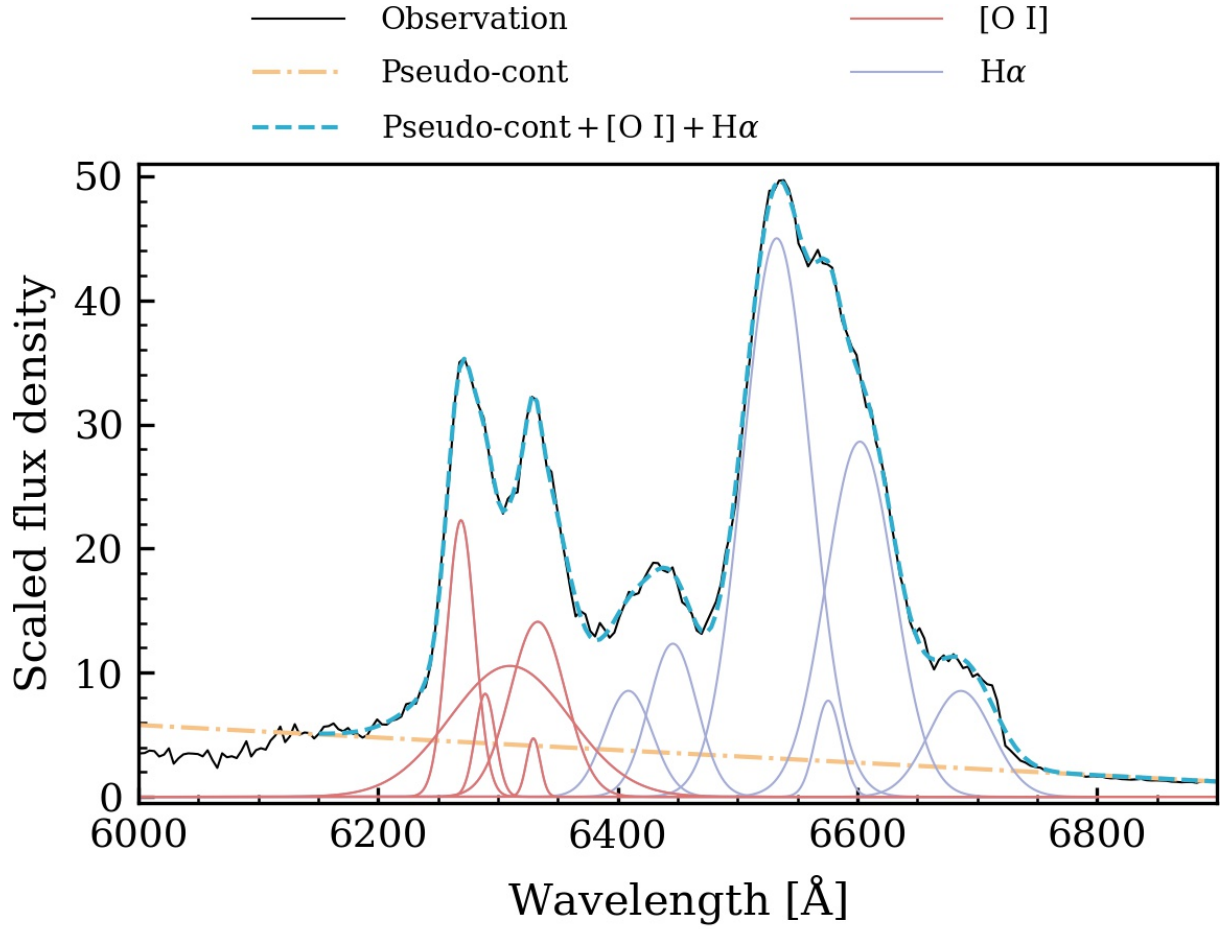
Appendix B: Fitting [O I] + H α with Multiple Gaussians

Fig. B.1. The [O I] + H α profile of SN 2023ixf at day 298. The observed spectrum (black solid line) is approximated by the dashed light-blue line, which consists of a pseudocontinuum (orange dot-dashed line), five Gaussian components of [O I] (solid red lines), and five Gaussian components of H α (solid dark-blue lines).